



## EGYPT JAPAN UNIVERSITY OF SCIENCE AND TECHNOLOGY

BACHELOR'S DEGREE IN MECHATRONICS AND  
ROBOTICS ENGINEERING

---

# Design and Development of Calibration System for MEMS Gas Meter

Graduation Project 2 Thesis

*Authors:*

Abdelrhman Abdelkader  
Ibrahim Gomaa  
Mahmoud Kataya  
Mohab El-Dean Yasser  
Mohamed Maher  
Mohamed Alaa  
Pierre Ihab  
Youssef Ahmed Hussein

*Supervisor:*  
**Prof. Ahmed Rashad  
Fathelbab**

*In Collaboration With:*  
**NeoSpectra Si-ware**

# Acknowledgments

We would like to express our deepest gratitude to Prof. Ahmed Rashad Fathelbab for his invaluable guidance, unwavering support, and insightful direction throughout this project. His expertise, encouragement, and dedication were instrumental in bringing this work to fruition. Without his mentorship, this project would not have been possible. We are also profoundly grateful to the Si-Ware Company team for their exceptional cooperation, technical expertise, and provision of resources, which enabled the development and testing of the MEMS gas sensor prototype. Their contributions were pivotal to the success of this endeavor. Finally, we extend our sincere appreciation to all individuals and organizations whose support, directly or indirectly, made this work achievable. Their collective efforts have been indispensable to the completion of this project.

**EGYPT JAPAN UNIVERSITY  
OF SCIENCE AND TECHNOLOGY**

*Abstract*

Mechatronics and Robotics Engineering

**Design and Development of Calibration System for MEMS Gas Meter**

by Abdelrhman Abdelkader  
 Ibrahim Gomaa  
 Mahmoud Kataya  
 Mohab El-Dean Yasser  
 Mohamed Maher  
 Mohamed Alaa  
 Pierre Ihab  
 Youssef Ahmed Hussein

The combination of micro electromechanical systems (MEMS) with infrared (IR) spectroscopy technology produces compact gas detection equipment that uses minimal energy. The sensors demonstrate increased sensitivity to external environmental factors including heat variations together with mechanical vibrations alongside structural material weakness that ultimately degrades measurement precision. This research develops an IR gas sensor based on MEMS technology with active thermal control and vibration suppression systems for superior reliability in drone and mobile robotic applications.

An integrated thermal management solution contains thermoelectric coolers (TECs) which work with a heat dissipation system that combines heat pipes and thermal interface materials (TIMs) and a heat sink to control thermal fluctuations. The vibration management system which integrates damping components with the sensor uses a structural design to reduce external vibrations that generate noise. The fiber glass-built mechanical enclosure meets industry standards that ensure operational durability because it follows relevant operating stress criteria.

This research identifies essential factors that help advance MEMS-based IR gas sensors while boosting their reliability and performance readiness for operational use. The established design methodology creates an essential basis for experience-based testing and enhancement during upcoming scientific investigations.

# Contents

<b>Acknowledgments</b>	<b>i</b>
<b>Abstract</b>	<b>i</b>
<b>1 Introduction</b>	<b>1</b>
1.1 Challenges Faced . . . . .	2
1.2 Objectives . . . . .	3
1.2.1 Thermal Team Objectives . . . . .	3
1.2.2 Vibration Management Team Objectives . . . . .	3
1.2.3 Mechanical Design and Certification Team Objectives . . . . .	3
<b>2 Literature Review</b>	<b>4</b>
2.1 Thermal Management in Gas Sensors . . . . .	4
2.2 Vibration Management in Spectroscopy Sensors . . . . .	4
2.3 Mechanical Design and Certification of Related Projects . . . . .	5
2.4 Integration of Multidisciplinary Approaches . . . . .	7
<b>3 Methodology</b>	<b>8</b>
3.1 Introduction . . . . .	8
3.2 Thermal Management Team . . . . .	8
3.2.1 Introduction . . . . .	8
3.2.2 Cooling Techniques . . . . .	8
3.2.3 Thermoelectric Cooler (TEC) . . . . .	9
Thermoelectric Cooling and Seebeck Effect . . . . .	9
3.2.4 Analogy Between Thermal and Electrical Circuits . . . . .	9
3.2.5 Analysis of TEC using LTspice . . . . .	10
3.2.6 Calculation of Parameters from Manufacturer's Datasheets	10
3.2.7 Fundamental Calculations and Thermodynamic Principles: . . . . .	11
3.2.8 The Schematic of the circuit and its Equivalent Scheme: . . . . .	11
The Basic Circuit: . . . . .	12
The Modified Equivalent Circuit: . . . . .	13
3.2.9 Model Construction: . . . . .	14
Simulation and Analysis . . . . .	14
3.2.10 Heat Dissipation System . . . . .	14
Thermal Vias for Enhanced Heat Transfer . . . . .	15
Aluminum Block as a Thermal Interface Material (TIM) . . . . .	15
Heat Pipes and Brazing Technique . . . . .	16
Heat Sink Design . . . . .	17
3.3 Vibration Management Team . . . . .	18
3.3.1 Sources of Vibration in drones . . . . .	18
<b>Motor and Propeller Rotation</b> . . . . .	18
<b>Aerodynamic Forces</b> . . . . .	18

<b>Structural Resonance</b>	18
Payload Movement	19
<b>Internal Components</b>	19
3.3.2 Material Selection	19
Silicone Rubber	19
<b>Polydimethylsiloxane (PDMS)</b>	20
Chemical Stability	20
Why do we choose PDMS?	20
3.3.3 Comparison Between Vertical and Tilted Plate	20
1. Orientation and Definition	20
2. Solar Energy Application	21
3. Heat Transfer	21
4. Fluid Dynamics	21
5. Structural Design	22
6. Applications in Renewable Energy	22
7. Aerodynamics:	22
8. Maintenance:	23
9. Environmental Interaction	23
3.3.4 Experimental Setup	24
I. Setup description	24
II. The measuring system holder	25
3.4 Mechanical Design Team	36
3.4.1 Responsibilities of Mechanical Design Team	36
3.4.2 Component Design and Mounting Techniques	36
Gas Chamber Design	36
Gas Chamber Cover Design	37
Chassis Design	40
Light Source Mount Design	40
Lens Mount Design	41
3.4.3 Pump Selection	41
Hose, Hose Clamps, and Quick Connectors	42
3.4.4 PCB Sensor Mount	43
3.4.5 Final Assembly	44
3.4.6 Material Selection	45
<b>4 Results</b>	46
4.1 Thermal Management Team:	46
4.1.1 Model Specification:	46
4.1.2 The Circuit:	47
Seebeck Effect Circuit:	48
The Main Circuit:	48
4.1.3 The Simulation:	49
Datasheet:	50
Closed Loop Circuit:	51
Important Notes:	53
4.1.4 Heat Dissipation System Calculations	55
Heat Loads, $Q_h$ and $Q_c$	56
4.2 Vibration Team Results	58
1) PSD data of dji 600 in x -axis	62
2) PSD data of DJI 100 in x -axis	64
Discussion	66

Key Observations . . . . .	67
Conclusion . . . . .	67
4.3 Mechanical Design Results . . . . .	68
4.3.1 Overpressure Test . . . . .	68
4.3.2 Drop Test . . . . .	69
4.3.3 Vibration Analysis . . . . .	70
<b>5 Future work</b> . . . . .	<b>72</b>
5.1 Thermal Management Team . . . . .	72
5.2 Vibration Management Team . . . . .	72
5.3 Mechanical Design Team . . . . .	73
<b>6 Discussion and Conclusion</b> . . . . .	<b>75</b>
6.1 Discussion . . . . .	75
6.1.1 Vibration Analysis and Performance . . . . .	75
6.1.2 Thermal Management Effectiveness . . . . .	75
6.1.3 Mechanical Integrity and Certification Readiness . . . . .	76
6.2 Conclusion . . . . .	76
6.3 Future Directions . . . . .	76

# List of Figures

1.1 <i>Structure of Non-Dispersive Infrared Absorption Sensor</i> . . . . .	1
3.1 PCB . . . . .	8
3.2 TEC Structure . . . . .	11
3.3 Schematic Circuit . . . . .	12
3.4 Modified Equivalent Circuit . . . . .	13
3.5 Heat-Flowchart . . . . .	14
3.6 Thermal Via Design . . . . .	15
3.7 Aluminum Block (TIM) . . . . .	16
3.8 Heat Sink Design . . . . .	17
3.9 Materials Selection . . . . .	20
3.10 Experimental Setup . . . . .	24
3.11 Experimental Setup . . . . .	24
3.12 PMMA Holder . . . . .	26
3.13 Results for Silicon 21 . . . . .	27
3.14 Samples of Different Ratios . . . . .	27
3.15 Result of Samples . . . . .	28
3.16 Result of Samples . . . . .	28
3.17 PDM . . . . .	28
3.18 Resonance Frequency . . . . .	29
3.19 Results of Sample . . . . .	30
3.20 S-shaped . . . . .	34
3.21 Conical Form . . . . .	35
3.22 Cylindrical Form . . . . .	35
3.23 Gas Chamber Design . . . . .	36
3.24 2D Drawing of Gas Chamber . . . . .	37
3.25 Gas Chamber Cover . . . . .	37
3.26 2D Drawing of Gas Chamber Cover . . . . .	38
3.27 Gas Cover Retaining Ring for Mirror . . . . .	38
3.28 Cover Design Closeup . . . . .	39
3.29 Chamber with Cover . . . . .	39
3.30 Chasis Screws . . . . .	40
3.31 2D Drawing of Light Source Mount . . . . .	40
3.32 Light Mount Design . . . . .	40
3.33 Lens Fixation Design . . . . .	41
3.34 BTX B1C-090P24AN-03 miniature diaphragm pump . . . . .	41
3.35 Pump Design . . . . .	42
3.36 Hose . . . . .	42
3.37 Male Socket . . . . .	43
3.38 Sensor Mount . . . . .	43
3.39 PCB Mounted . . . . .	44
3.40 2D Drawing of PCB Spacers . . . . .	44

3.41 Final Assembly . . . . .	44
3.42 Final Assembly . . . . .	45
3.43 Full Sensor Body . . . . .	45
4.1 Circuit Design on LTspice . . . . .	47
4.2 Seebeck Effect Circuit . . . . .	48
4.3 Main Circuit . . . . .	49
4.4 Simulation Graph 1 . . . . .	49
4.5 Enter Caption . . . . .	50
4.6 Q <sub>h</sub> vs Operating Current Graph . . . . .	50
4.7 Closed Loop Circuit . . . . .	51
4.8 Output Circuit . . . . .	51
4.9 Closed Loop Results . . . . .	52
4.10 Closed Loop Results 2 . . . . .	52
4.11 Results of Pelteir Temperatures . . . . .	53
4.12 Operating Current Graph . . . . .	57
4.13 Operating Voltage Graph . . . . .	57
4.14 Drones in Experiments . . . . .	59
4.15 DJI 600 . . . . .	60
4.16 DJI 600 . . . . .	60
4.17 DJI 100 . . . . .	61
4.18 DJI 100 . . . . .	61
4.19 Damper . . . . .	62
4.20 Comparison of PSD (g <sup>2</sup> /Hz) data before using damper and PSD(m <sup>2</sup> /Hz) after using damper at random vibration test for Dji matrice 600 for x axis . . . . .	62
4.21 Deflection in Y-axis . . . . .	63
4.22 Deflection in X-axis . . . . .	63
4.23 Deflection in Z-axis . . . . .	63
4.24 Comparison of PSD (g <sup>2</sup> /Hz) data before using damper and PSD(m <sup>2</sup> /Hz) after using damper at random vibration test for Dji matrice 100 for x axis . . . . .	64
4.25 Z-Deflection . . . . .	64
4.26 Y-Deflection . . . . .	65
4.27 X-Deflection . . . . .	65
4.28 Forces Applied . . . . .	68
4.29 Stress Results in Overpressure Test . . . . .	69
4.30 Displacement Results in Overpressure Test . . . . .	69
4.31 Displacement Results in Drop Test . . . . .	70
4.32 Stress Results in Drop Test . . . . .	70
4.33 Natural Frequencies of Laser Mount . . . . .	71
4.34 Natural Frequencies of PCB Mount . . . . .	71
4.35 Natural Frequencies of Lens Mount . . . . .	71

## Chapter 1

# Introduction

Gas sensors have become an integral part of modern sensing applications, utilized across a broad spectrum of industries, including but not limited to environmental studies, medicinal field applications, and industrial process control. The detection of gases through different sensing mechanisms, such as electrochemical, optical, or infrared (IR) spectroscopy, plays a very important role in increasing safety and efficiency. Among the many known methods is infrared spectroscopy, sensors based on this method also known as IR-Spectroscopy sensors, such as the micro electromechanical system (MEMs) sensor that is to be developed in this research have gathered a lot of attention in the past years due to their increased efficiency, low power consumption and their compact sizes. These sensors can effectively detect a wide range of gases and elements using the gas molecules specific vibrational profiles and frequencies to measure the absorption of an emitted infrared light at specific wavelengths and corresponding the received ray to the specific vibrational mode of the gas in question to determine it. However, despite these sensors' potential, their development raises numerous challenges that must be addressed to ensure accurate and reliable performance in real-world applications. This is because such a sensing method is very sensitive to many factors. Therefore, to have an industrially viable IR-spectroscopy sensor several factors need to be kept in check and under control.

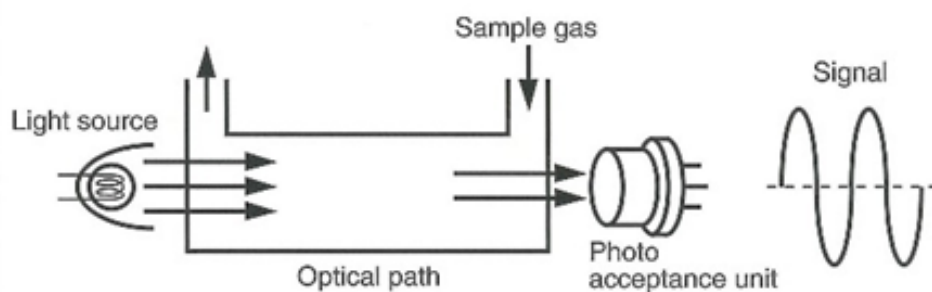


FIGURE 1.1: *Structure of Non-Dispersive Infrared Absorption Sensor*

## 1.1 Challenges Faced

The primary challenge that is to be addressed in this research in developing a MEMS-based IR gas sensor lies in the control and mitigation of the various factors that can negatively affect the sensing process. These are mainly temperature variations, mechanical vibrations and noise, as well as structural weaknesses in case of using the sensor with a different system such as drones or mobile robots to detect in remote places, the sensors' mechanical body also helps mitigate sensor degradation, or complete failure. To address these challenges, this thesis focuses on the design and development of a MEMS-based IR gas sensor with controlled temperature and vibration management, along with an optimized mechanical structure. Given that the target application for this sensor is in dynamic environments, such as drones or mobile robots, the sensor must be capable of maintaining accuracy despite the inherent challenges presented by these environments.

## 1.2 Objectives

### 1.2.1 Thermal Team Objectives

To develop a thermal management system that minimizes the impact of temperature variations, as well as prevent possible overheating problems. Moreover, create a thermal circuit that simulates and mimics how the proposed cooling system will operate.

### 1.2.2 Vibration Management Team Objectives

To design a vibration management system that stabilizes the sensor and minimizes the effects of exterior sources of noise and vibrations that may arise from integrating the sensor with mobile applications.

### 1.2.3 Mechanical Design and Certification Team Objectives

To create a mechanical design for the sensor body and enclosure that meets industry certifications and standards that prevent possible leakages of the gas being processed, while ensuring durability and robustness of the sensor body under operational stresses that are caused by the pumping of gas through the sensing chamber.

This study intends to enhance the reliability and accuracy of gas detection systems in on-field real-world applications through the precise control of thermal and vibrational influences. In addition, the mechanical design and certification aspects of the project ensure that the sensor meets necessary industry standards, enhancing its commercial viability.

The approach used in this study includes the creation of simulated-theoretical, vibrational, and mechanical models. The thermal management system regulates the sensor's temperature using advanced materials and heat-dissipation techniques, whilst the vibration management system employs stabilization methods like dampening materials and structural strengthening to reduce vibration-related noise. The mechanical design and certification process will begin with the creation of a strong sensor enclosure, followed by testing to ensure that the sensor meets applicable industry performance and durability standards.

The rest of the thesis is organized as follows: Chapter 2 presents a thorough assessment of the literature on MEMS-based gas sensors and the unique issues associated with IR spectroscopy. Chapter 3 describes the system design and technique used to develop the sensor. Chapter 4 presents the results of the design, including thermal and vibration testing, as well as mechanical stress testing. Finally, Chapter 5 discusses the conclusions and provides recommendations for future work in this field.

## Chapter 2

# Literature Review

### 2.1 Thermal Management in Gas Sensors

The accuracy and reliability of gas sensors strongly depend upon their thermal stability state. Temperature variations change the optical behavior of materials during IR spectroscopy measurements thereby producing inaccurate results. Excessive temperature changes lead to IR sensors drifts primarily through the alteration of optical components' refractive index and sensor architecture expansion alongside sensor detection sensitivity fluctuation [1] [2].

Different approaches have been developed to address the ongoing problems in these systems. Active cooling mechanisms that use thermoelectric coolers have become standard practice for stabilizing temperatures across IR spectroscopy systems according to reports from [3]. These precise temperature control systems introduce technical limitations such as bulk size and high-power requirements, so they work poorly for mobile sensor applications. The field of passive thermal management continues to focus on studies evaluating heat sinks alongside thermal insulation and advanced materials that demonstrate low thermal conductivity [4]. Silicon and silicon nitride offer promising possibilities for MEMS-based sensors because of the combination of favorable thermal properties alongside compatibility with established micro-fabrication approaches [5]. Real-time measurement error correction through thermal compensation algorithms was developed by researchers [6].

### 2.2 Vibration Management in Spectroscopy Sensors

Energy dissipation through the spectrum presents fundamental limitations for IR spectroscopy sensors operating within moving scope systems. Fabricated vibrations create signal noise through three principal mechanisms which include optical component misalignment and light path instability as well as the spectral data warp. Membrane electronic devices suffer greatly from vibrations because their minimal size results in weak structural damping capability compared to larger platforms. [7]

The research into vibration mitigation explores techniques combining passive elements with active interventions. Passive vibration isolation implements viscoelastic polymers together with mechanical design elements that minimize vibrational energy transmission [8]. Portable gas sensors frequently use rubber gaskets together with foam-based isolators to minimize

vibrational noise according to research in [9]. Real-time vibration counteraction during active vibration control happens through sensor-actuator systems. MEMS devices now incorporate piezoelectric actuators to stabilize their sensor platforms while maintaining alignment according to research [10]. Insightful optical designs incorporate orthogonal beam paths to overcome vibrational disturbances by conducting parallel differential measurements which eliminate noise artifacts [11].

## 2.3 Mechanical Design and Certification of Related Projects

### Gas Chamber Design

- "Design and application of a high-pressure combustion chamber for ..." [12]

This paper describes the design of a high-pressure combustion chamber with a cylindrical geometry, similar to our gas chamber design. The study demonstrates how cylindrical chambers can be engineered to handle high pressures while maintaining accessibility and lightweight properties.

- Cylindrical design can contain high pressures, up to 200 bar.
- The compact, flangeless, and weldless design allows easy access.
- Material selection balances corrosion resistance and structural strength.
- Finite element method stress analysis ensures safety and reliability.
- A safety factor of 2 is applied for containment pressure.

- "GASKET HANDBOOK 1st Edition" [13]

This handbook focuses on two critical aspects of gas chamber design beyond geometry: sealing and material selection.

- Gasket material selection is crucial for effective sealing in a pressurized system.
- The work discusses different gasket materials, including elastomers, metals, and composites like PTFE, highlighting their applications.
- Gaskets must be resilient enough to accommodate flange imperfections.
- Important factors in seal design:
  - \* Overcoming minor alignment issues and flange imperfections.
  - \* Consideration of operating temperature and pressure ranges.

### Choice of Proper Mounting Techniques

- "Optomechanical Design and Analysis" [14]

This book provides practical information on methods for mounting optical components, which are relevant for our MEMS gas sensor.

- Retaining rings: Secure lenses while allowing thermal expansion.

- Flexure mounts: Prevent stress and deformation in optics.
  - Adhesive bonding: Useful in compact construction; requires careful adhesive selection.
  - Kinematic mounts: Ensure highly accurate and stable lens positioning.
  - Threaded mounts: Provide adjustability but may introduce stress.
- "MEMS Packaging" [15]

This book focuses on MEMS device mounting techniques and general challenges in MEMS packaging.

- Secure die attachment methods for PCB mounting.
- Hermetic sealing techniques for environmental protection.
- Wire bonding and flip-chip bonding for electrical connections.
- Stress isolation strategies to safeguard sensitive MEMS components.

## Material Selection

- "Chemical Resistance and Mechanical Properties of Glass Fiber-Reinforced Plastic Pipes for Oil, Gas, and Power-Plant Applications" [16]

This study reviews the properties of glass fiber-reinforced plastic (GFRP) pipes used in oil and gas applications, focusing on their chemical resistance and mechanical behavior.

- GFRP's resistance to various industrial gases.
- Mechanical properties, including tensile strength and elasticity modulus.
- Long-term performance in harsh chemical environments.
- Degradation of properties due to chemical exposure.
- Suitability for high-pressure gas containment.

## Certification Compliance

- "ATEX Guidelines - 4th Edition" [17]

This book provides a comprehensive guide to ATEX Directive requirements for equipment used in potentially explosive atmospheres. It is highly relevant to our project, detailing the necessary safety considerations for ATEX certification.

- Product categorization based on the intended use environment.
- Essential health and safety requirements related to design and construction.
- Risk assessment and hazard analysis procedures.
- Documentation requirements, including technical files and user manuals.
- Conformity assessment procedures and CE marking.

- "IP67 Waterproof Leak Testing: What You Need to Know" [18]

This article provides practical insights into achieving and performing tests for IP67 certification, crucial for our gas sensor's environmental protection.

- Complete dust-tight design (IP6X).
- Waterproofing for 1-meter submersion for 30 minutes (IPX7).
- Sealed device fill volume testing process.
- Testing methodologies: Pressure Decay and Differential Pressure Decay.
- Material selection for effective sealing.

## 2.4 Integration of Multidisciplinary Approaches

The creation of MEMS-based gas sensors depends on essential multidisciplinary integration among methods for temperature and vibrational and mechanical stress management. Recent scientific studies prove sensor designs can leverage joint implementation of these methods to deliver reliable performance. Zhang et al. [19] built an improved MEMS-based IR gas sensor that used a thermally stable substrate and vibration-damping mounts with a reinforced enclosure to show better accuracy and field reliability. Simulation tools have evolved to let researchers analyze thermal and mechanical effects while modeling vibrational dynamics for improved design optimization as part of fabrication preparation [20].

## Chapter 3

# Methodology

### 3.1 Introduction

In this section, the steps taken by each team to work around and solve their challenges to achieve the objectives mentioned earlier in 1 . Therefore, this chapter structure will be split into three sections, each covering how the obstacle was dealt with.

### 3.2 Thermal Management Team

#### 3.2.1 Introduction

Firstly, it was important to identify our heat sources and choose a way to prevent these heat sources from causing any negative effects on the operation of the spectroscopy sensor. In our case, the heat sources were the circuitry around the sensor as well as the IR rays reflected to the sensor.

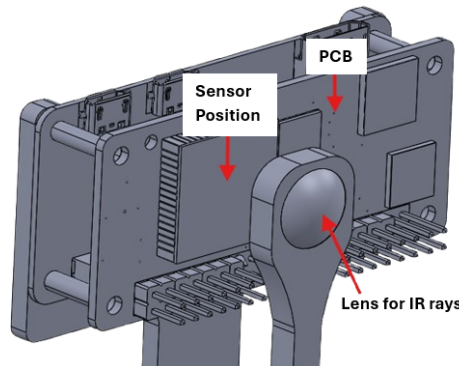


FIGURE 3.1: PCB

Other external heat sources could arise if the sensor were integrated with a drone operating in sunny, warm weather.

#### 3.2.2 Cooling Techniques

Given the sensor's sensitivity to vibrations and noise, conventional cooling methods such as fans were unsuitable due to the vibrations they introduce. Additionally, the compact size of the sensor and its use of MEMS technology ruled out large-scale cooling techniques. Therefore, a solid-state cooling technique was preferred to avoid moving parts that could introduce failure or fatigue.

Cooling methods are classified into conventional and non-conventional techniques. Conventional cooling methods, such as air conditioning and liquid cooling, rely on phase change and convective heat transfer to regulate temperature. These methods, while effective, are bulky and dependent on refrigerants. Non-conventional cooling methods, such as evaporative cooling and thermoelectric cooling, utilize solid-state mechanisms to transfer heat and are more compact, environmentally friendly, and suitable for applications requiring precise cooling.

### 3.2.3 Thermoelectric Cooler (TEC)

We chose the Thermoelectric Cooler (TEC) for its compact size, reliability, and precise temperature control. Unlike conventional cooling methods, TECs operate without moving parts, making them easy to utilize in any project and offering smooth and easy maintenance.

#### Thermoelectric Cooling and Seebeck Effect

Thermoelectric cooling (TEC) is based on the Peltier effect, where an electric current is applied to a thermoelectric unit, causing heat to move from one side to the other. This leads to cooling on one surface and heating on the other surface. This principle is closely related to the Seebeck effect, where a temperature difference across a thermoelectric material generates an electrical voltage, enabling power generation in reverse operation.

### 3.2.4 Analogy Between Thermal and Electrical Circuits

The analogy of a thermal system into an electrical circuit is based on the mathematical similarities between heat transfer and electrical conduction. In both systems, we have a driving potential (temperature difference or voltage difference) that induces a flow quantity (heat flow or electrical current) and is opposed by a resistive element (thermal or electrical resistance).

Fourier's Law of heat conduction relates heat flow to the temperature difference using thermal resistance, which is structurally identical to Ohm's Law for electrical circuits.

TABLE 3.1: Analogy Between Thermal and Electrical Systems

Thermal System	Electrical System	Explanation
Heat Flow Rate ( $Q$ ) [W]	Electric Current ( $I$ ) [A]	Heat flow corresponds to the movement of charge in a circuit.
Temperature ( $T$ ) [ $^{\circ}\text{C}$ or K]	Voltage (V) [V]	Temperature difference drives heat flow, same as voltage difference drives current.
Thermal Resistance ( $R$ ) [K/W]	Electrical Resistance ( $R$ ) []	The resistance of a material to heat flow is like an electrical resistor limiting current.
Thermal Capacitance ( $C$ ) [J/K]	Electrical Capacitance ( $C$ ) [F]	A material's ability to store heat corresponds to an electrical capacitor storing charge.

### 3.2.5 Analysis of TEC using LTspice

In LTspice, the TEC is modeled by an equivalent electrical circuit, where thermal resistance and thermal capacitance are represented using resistors and capacitors. The Peltier effect is simulated using controlled current sources, while the Seebeck effect is modeled as a voltage source. A Thermal RC system captures heat transfer dynamics, offering simulations of steady-state, transient, and small-signal AC responses.

### 3.2.6 Calculation of Parameters from Manufacturer's Datasheets

The manufacturers of TECs use the following parameters to specify their product:

- $\Delta T_{\max}$ : The largest temperature differential that can be obtained between the hot and cold ceramic plates of a TEC for a given level of  $T_h$ .
- $I_{\max}$ : The input current (A) which will produce the maximum possible  $\Delta T$ .
- $V_{\max}$ : The DC voltage (V) that will deliver the maximum possible  $\Delta T$  at the supplied  $I_{\max}$ .
- $Q_{\max}$ : The maximum amount of heat (W) that can be absorbed at the TEC's cold plate at  $I_{\max}$  and at a  $\Delta T$  equal to 0.

$Q_{\max}$  is not the maximum possible amount of heat that can be overseen by the TEC, it is rather the heat flow corresponding to the current  $I_{\max}$ .

$Q_{opt}$  is the maximum amount of heat that can be absorbed at the TECs cold plate for a T equal to 0.

Using these notations the characteristic parameters of the TEC can be derived as follows:

$$\Delta T_{\max} = T_h + \frac{1 - \sqrt{1+2T_hZ}}{Z}$$

$$I_{\max} = \frac{\sqrt{1+2T_hZ}-1}{\alpha_m \Theta_m}$$

$$V_{\max} = \alpha_m T_h$$

$$Q_{\max} = \frac{\sqrt{1+2T_hZ}(\sqrt{1+2T_hZ}-1)^2}{2\Theta_m Z}$$

$$I_{opt} = \frac{\alpha_m T_h}{R_m}$$

$$Q_{opt} = \frac{\alpha_m^2 T_h^2}{2R_m}$$

Where  $Z$  is the figure of merit of the TEC, which is labelled as  $Z = \text{mm/Rm}$

### 3.2.7 Fundamental Calculations and Thermodynamic Principles:

Through established thermal to electrical circuit analogies researchers can effectively simulate and analyze thermoelectric systems. The simulation initiation needs computation of the system-controlling key constants. Thermoelectric module energy distribution obeys the First Law of Thermodynamics rules about energy conservation. Specifically, the energy balance must be established between the two distinct junctions of the module: the absorbing junction (a) and the emitting junction (e). The system equilibrium derives from three operational processes and physical gradients of heat and electrical conversion within the system.

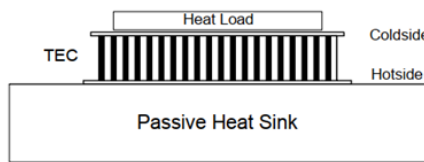


FIGURE 3.2: TEC Structure

For the absorbing side,, the heat absorbed would be:

$$q_a = \frac{\Delta T}{\Theta_m} + \alpha_m T_a I - \frac{I^2 R_m}{2}. \quad (3.1)$$

and for the emitting side the heat emitted is:

$$q_e = \frac{\Delta T}{\Theta_m} + \alpha_m T_e I + \frac{I^2 R_m}{2} \quad (3.2)$$

For the thermal analogy we need to calculate some additional variables:

$$\alpha_m = \alpha \times N \quad (3.3)$$

$$R_m = RN \quad (3.4)$$

$$\Theta_m = \Theta / N \quad (3.5)$$

Where alpha m is the Seebeck coefficient and Rm is the electrical resistance of the system or the module and N is the number of couples, Ta and Te are the temperatures of the (a) and (e) sides in Kelvin, and finally the Theta m is the Thermal Resistance of the couple in the direction of the heat flow and Delta T is the difference between Te and Ta (Te-Ta).

There is also an effect that is still present in the circuit or model called the Thompson effect, but it is neglected because of having a very small value.

Moreover, the electrical potential difference (V) is calculated from:

$$V = \alpha_m T_e - \alpha_m T_a = \alpha_m \Delta T. \quad (3.6)$$

### 3.2.8 The Schematic of the circuit and its Equivalent Scheme:

The Thermoelectric Cooler (TEC) circuit is typically represented using electrical components that model its thermal and electrical behavior. It is a

widely accepted practice in one-dimensional heat transfer analysis to employ an equivalent electrical circuit analogy. This approach, which will be elaborated upon later, was adopted in this study to characterize the Thermoelectric Module (TEM) system. TEM involves multiple forms of energy, including thermal and electrical energy, which interact within the system.

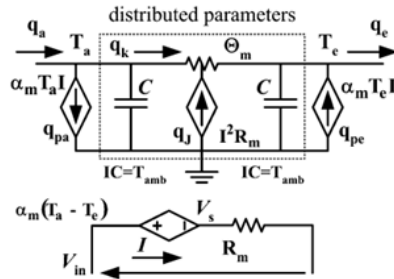


FIGURE 3.3: Schematic Circuit

In this methodology, all non-electrical processes and components are represented as electrical analogies. Specifically, these components are transformed into electrically dependent sources and elements, such as voltage and current sources, resistors, and capacitors, which correspond to thermal resistances, heat fluxes, and thermal capacitance, respectively. The interconnections between these components are carefully defined to construct a comprehensive thermoelectric model of the TEC. This transformation ultimately results in a purely electrical circuit that accurately describes the behavior of the thermoelectric system.

### The Basic Circuit:

This figure shows the first interconnections between the Thermo-electrical circuit of the TEC system to be constructed as fully electrical circuit to be simulated and to clarify how to change the thermal components to the electrical components a table will be shown later Table 2.

This network is usually used to represent heat conduction transfer in solids.  $q$  is the source of joule heating of TEC. Peltier cooling on the absorbing side  $q_{pa}$  and Peltier heating on the heating side or the emitting side. The electrical part consists of the voltage source  $V_s$  and the electrical resistance  $R_m$ . All capacitors in the circuit have the initial value =  $T_{amb}$ .

THERMAL TO ELECTRICAL ANALOGY			
Thermal quantities	Units	Analogous Electrical Quantities	Units
Heat, $q$	W	Current, $I$	A
Temperature, $T$	K	Voltage, $V$	V
Thermal Resistance, $\Theta$	K/W	Resistance, $R$	$\Omega$
Heat capacity, $C$	J/K	Capacity, $C$	F
Absolute zero temperature	0 K	Ground	0 V

TABLE 3.2: Thermal to Electrical Analogy

### The Modified Equivalent Circuit:

1. The upper dependent voltage source resembles the Seebeck effect.
2. The Resistance next to this source  $m$  is the Thermal resistance of the TEC.
3. The independent circuit shown detached from the circuit is has dependent sources that affect the whole circuit or TEC model as the current  $I$  from the voltage source drawn down in the circuit is affecting the Peltier effect so if the current has increased the Peltier effect will decrease.
4. The current source with value  $I \times V$  is the power dissipated by the electrical circuit so it could be considered as a waste that has to be removed from the hot side.
5. The left side of the  $T_a$  is considered as a Cold Side.
6. The Right side is considered as the Hot side.

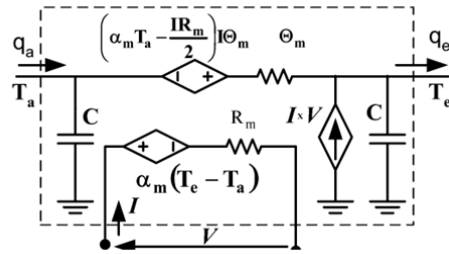


FIGURE 3.4: Modified Equivalent Circuit

### Parameter Extraction from Manufacturer Data

**1) Data Collection:** Manufacturer datasheets present essential operational parameters consisting of maximum temperature differential ( $T_{max}$ ), maximum current ( $I_{max}$ ), maximum voltage ( $V_{max}$ ) and maximum heat absorption ( $Q_{max}$ ) to define TEC operational boundaries.

**2) Parameter Calculation:** Using the relationships derived from the thermoelectric principles, the model parameters are calculated. These include the Seebeck coefficient ( $\alpha_m$ ) electrical resistance ( $R_m$ ) and thermal resistance( $m$ ) The equations used are:

$$R_m = \frac{V_{max}(T_h - \Delta T_{max})}{I_{max} T_h} [\Omega]$$

$$\Theta_m = \frac{\Delta T_{max}}{I_{max} V_{max} (T_h - \Delta T_{max})} \cdot \frac{2T_h}{1} \left[ \frac{K}{W} \right]$$

$$\alpha_m = \frac{V_{max}}{T_h} \left[ \frac{V}{K} \right] . (3.7)$$

**3) Validation:** The parameters get verified using manufacturer performance plots to validate accuracy levels.

### 3.2.9 Model Construction:

**1-Equivalent Circuit Design:** The analog electrical circuit model represents the TEC through combinations of resistors and capacitors along with dependent sources. The circuit representation translates the thermal and electrical behavior of TEC through the mechanisms of heat exchange and Peltier effects.

**2-SPICE Implementation:** Circuits designed for equivalent function execute through SPICE hardware to enable both transient and steady state processes. The model incorporates initial-state specifications combined with adjustable parameter values to assess TEC operational characteristics across different operating scenarios.

## Simulation and Analysis

**1-Steady-State Analysis:** The simulation performs DC sweep tests to produce representations of the TEC performance data. The analysis helps determine the connection between current ratings with voltage supply levels and temperature differentials.

**2-Transient Analysis:** The TEC's dynamic performance is examined through time-domain simulation tests. This system follows temperature relaxation dynamics as voltage measurements increase and then decrease after an applied steady potential.

**3-Small-Signal Analysis:** Small-signal transfer functions generated through this model enable designers to create feedback control systems. The computation of a transfer function requires SPICE to execute Alternating current (AC) analysis methods. [21]

### 3.2.10 Heat Dissipation System

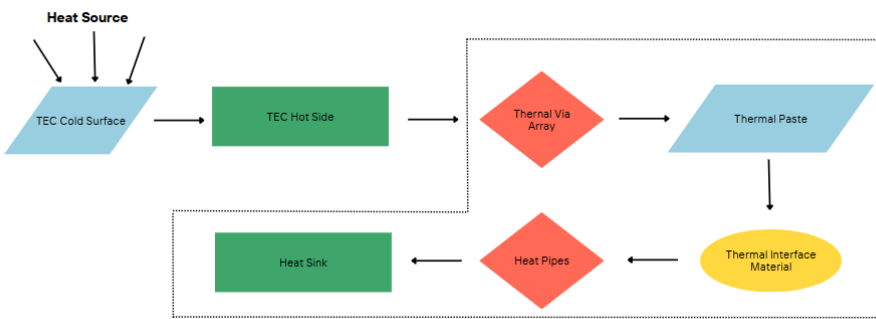


FIGURE 3.5: Heat-Flowchart

Efficient heat dissipation on the hot side is critical to maintaining performance and preventing overheating. A robust cooling system was designed using a combination of a heat sink, heat pipes, and an aluminum block to function as our thermal interface material (TIM). The system

includes an aluminum heat sink to increase the surface area for better heat transfer.

### Thermal Vias for Enhanced Heat Transfer

Thermal vias are another way to ensure heat dissipation, used by adding a custom layer beneath the Peltier sensor. Thermal via are small, conductive pathways filled with materials like copper to create a path for heat to travel vertically, in this case this was done to move the heat from one side of the PCB to the other, allowing for more space to work, as well as moving the heat away from the sensor. To make sure the designed array was efficient as possible, a standard calculator that aids in the design of thermal via array was utilized to try and find the dimensions that best fit our space right under the TEC while maintaining the lowest thermal resistance possible. [22]

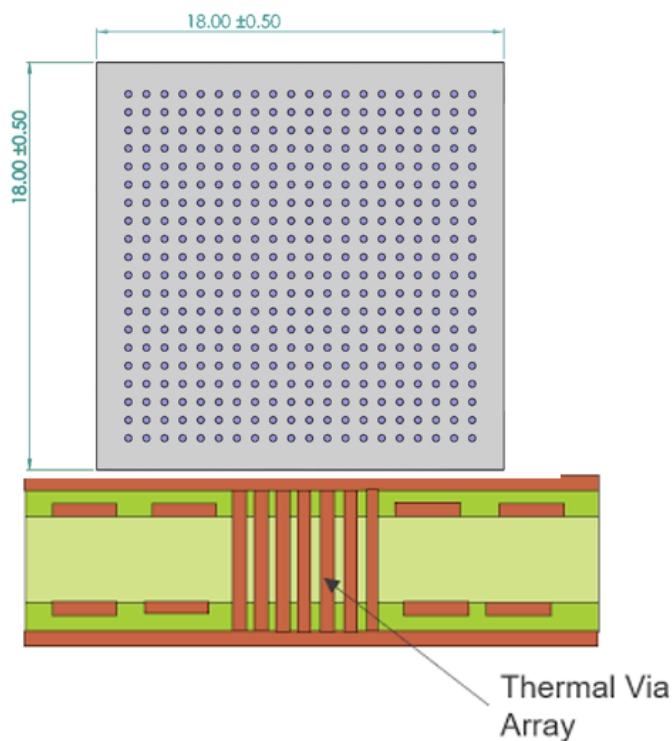


FIGURE 3.6: Thermal Via Design

Once the heat is transferred to the other side of the board, the next step is to work on dissipating this heat all the way to the heat sink where it will be dissipated to the air.

### Aluminum Block as a Thermal Interface Material (TIM)

The next step was to choose a thermal interface material (TIM) that helps connect the system together and transfer the heat efficiently to the heat pipes, therefore an aluminum block with grooves made specifically for the heat pipes is chosen, this is clearly shown in the following figure:

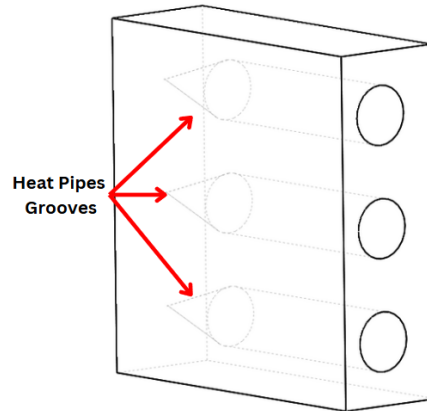


FIGURE 3.7: Aluminum Block (TIM)

In our system, the aluminum block was suggested for two purposes: It acted as a structural component to hold the heat pipes in place and as a thermal interface material (TIM). The block was placed directly on the hot side of the Peltier sensor, ensuring direct contact for efficient heat transfer. Aluminum was chosen for its high thermal conductivity.

However, to make sure the transfer between the thermal via and the aluminum block is efficient, a thermal paste layer must be added so that it fills in the air gaps that may be present between the thermal via array and the aluminum block as air is a poor conductor of heat and would add thermal resistance that is to be avoided.

### **Heat Pipes and Braze Technique**

Heat pipes were used in the system to transfer the heat from the bottom side of the PCB where the aluminum block is present to the heat sink. These pipes transfer heat with the use of phase change between evaporation and condensation to move heat away from the source. The heat pipes are attached to the aluminum block using a braze technique. Braze is the melting of a filler metal (such as a copper-silver alloy) to create a strong, conductive bond between the heat pipes and the aluminum block. This method ensures durability and efficient heat transfer from the aluminum block to the heat pipes, due to the fact that there is a consistent layer of filler metal holding and connecting the heat pipes. [23] Since the heat pipes chosen are 150mm long this length is split into three sections as follows: a 40mm long evaporator section, 70mm midsection, and a condensation section of 40mm long.

The type of heat pipes used is also a very important detail to make sure they are both suitable for the dimensions of the sensor enclosure but are also capable of carrying the heat load without overheating. The type of heat pipe chosen was the Wakefield Thermal (124643 ROUND, COPPER HEAT PIPE, SINTERED, 3mmX150mm) [24]. Moreover, the dimensions of the aluminum block allowed for the placement of three of these heat pipes so that the heat load is distributed among them, this is also visible in the aluminum block figure.

### Heat Sink Design

Finally, the last step of the heat dissipation system is the heat sink which is the part that is responsible for increasing the surface area exposed to the air. This is the most important part of the dissipation system as it plays a crucial role in the calculations of thermal resistances of the whole system. The two most important factors that influence the thermal resistance of the heat sink are the dimensions of the heat sink, these include but are not limited to the length, width, thickness of plate, fin length and design, the other factor is the material selection which is usually either copper or aluminum. For this project an aluminum heat sink was chosen as it is lighter and cheaper. This heatsink has a width of 24mm and a length of 44.25mm, this length is made so that it can accommodate the whole length of the condensation section of the heat pipes. The base is 4mm thick so that it can easily contain the heat pipes in the same way it was mentioned earlier, by brazing, finally the fins are 5.2mm long and the surface has a total of 80 small fins that increase the surface area even further.

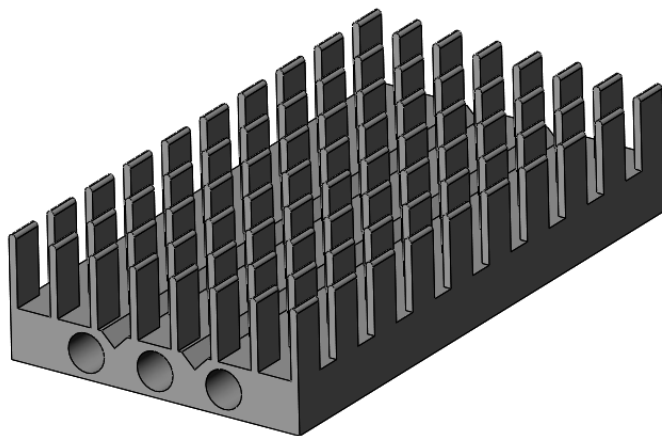


FIGURE 3.8: Heat Sink Design

### 3.3 Vibration Management Team

To preserve performance and steadiness, our vibration team has been working towards researching and improving drone vibration profiles. With significant efforts in creating flawless plates and silicone dampers, we have been working intensively towards overcoming vibration-related issues. By improving these factors, we work towards creating an ideal environment with zero unnecessary vibrations, improving dependability in a drone, and providing flawless performance with no performance-related complications.

#### 3.3.1 Sources of Vibration in drones

##### Motor and Propeller Rotation

The main source of vibrations in UAVs is the propeller and motor motion. These vibrations may be made worse by misaligned motors or imbalanced propeller blades [25], for instance, discovered that two rotating propellers can produce shock forces of up to 14 G in both vertical and horizontal directions while in flight. These motor-generated vibrations can also interfere with the UAV's electronic systems, leading to malfunctions or inaccurate sensor data [26]. To reduce vibrations and ensure smooth operation, it is essential to properly balance the propellers and motors [27]. Regular calibration and maintenance are essential to avoid excessive vibrations, which can cause premature wear of the UAV's airframe.

##### Aerodynamic Forces

Rapid turbulence and oscillations during flight can lead to aerodynamic vibrations caused by the wind and speed of the drone [28]. These stresses cause the drone's structure to be subjected to additional stresses, which alters the airflow around it. High-frequency vibrations caused by turbulence can degrade image quality, especially for cameras mounted on drones [29]. The overall performance of the UAV is improved by using PID controllers and other advanced flight control algorithms to help regulate directional vibrations [30]. These vibrations can be significantly reduced using effective design strategies that improve airflow efficiency and reduce aerodynamic drag.

##### Structural Resonance

The drone frame and other components may resonate at specific frequencies, causing vibrations to become more intense and perhaps resulting in structural failure [31]. This resonance happens when the inherent frequency of the drone's components is matched by external forces, increasing the vibration amplitude. To ensure the safety of the drone structure, engineers use modal analysis techniques to detect and reduce these resonant frequencies [32]. By identifying the inherent frequencies of the drone structure, the modal shapes, and the damping ratios, modal analysis enables engineers to identify design flaws. Resonance-related failures can be reduced by addressing these issues through material selection and structural optimization.

### **Payload Movement**

Additional vibrations can occur due to unsecured payloads, especially in turbulent or violent movements [33]. The stability and control of a drone can be significantly affected by the movement of the payload in applications such as medical supply delivery. For example, drone flights have been shown to have more vibration than ground transportation, which can be dangerous for sensitive goods such as insulin, according to [33]. To reduce unwanted vibrations and maintain optimal flight performance, the payload must be securely secured. Fragile products can be protected during transport by designing specific payload compartments with vibration isolation techniques. Routine maintenance and inspection are also essential to ensure the reliability and efficiency of payload attachment mechanisms.

### **Internal Components**

Internal components such as batteries and electronic circuits can also cause vibrations, especially if they are not installed properly [34]. Premature wear can occur as a result of additional vibrations caused by loose connections or incorrectly placed parts. To extend the operating life of the drone and avoid vibrations caused by internal components, proper assembly and routine maintenance are required. The use of advanced materials, such as carbon fiber composites, can enhance structural integrity and reduce vibrations. For sensitive electronics, the addition of vibration isolation mounts can help reduce the impact of internal vibrations on the operation of the drone. The consequences of these vibrations can also be reduced through continuous monitoring and real-time adjustments made using sensors and control algorithms.

#### **3.3.2 Material Selection**

Material selection is an important factor in damper design. There are many types of materials that have the ability to damp exciting force.

##### **Silicone Rubber**

Silicone rubber offers several advantages for damper manufacturing:

- Greater tensile strength (3.5–6 MPa), can withstand higher forces without breaking.
- Lower deformation under load, maintaining shape under static/dynamic compression.
- Better elastic behavior, offering higher resilience.
- Temperature resistance: withstands up to 250°C.
- Excellent UV, oxidation, and chemical resistance.

### Polydimethylsiloxane (PDMS)

Polydimethylsiloxane is a crosslinked polymer, and stiffness can be controlled by varying the crosslinking density. For soft PDMS mixtures from 1:60 or 1:50 ratios of crosslinker to PDMS, Young's modulus measurements of 3 or 8 kPa, respectively.

#### Mechanical Properties.

Hardness and Elasticity: allows control over stiffness and damping characteristics by modifying mixing ratio(1:45 ), Lower shore hardness: Can be made softer compared to general silicone allowing better damping applications

#### High damping performance:

PDMS has viscoelastic behavior, It exhibits high energy dissipation at low frequencies which make it suitable for dampers

#### Easy Molding:

Low viscosity in liquid form which makes it easier to cast into complex shapes (S-Shape is our design)

No need for high temperature curing: PDMS cures at room temperature with a curing agent

Shrinkage: precision in final dimension

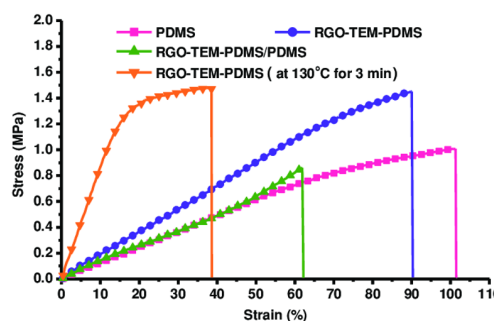


FIGURE 3.9: Materials Selection

### Chemical Stability

PDMS has excellent thermal stability (-40C - 200C), Resistance to moisture, Ultra-violet and oxidation, Good Chemical resistance to oils, solvents and environmental exposure [35]

#### Why do we choose PDMS?

Because PDMS Can Perform higher damping performance, dampers need to be softer and more flexible which mitigate with our requirements

### 3.3.3 Comparison Between Vertical and Tilted Plate

The following is a comparative analysis between a tilted plate and a vertical plate in relation to various areas of application, including solar energy, heat transfer, fluid dynamics, and structural engineering.

#### 1. Orientation and Definition

- Vertical Plate:

- Perpendicularly oriented plate, most commonly utilized in buildings, walls, and passive heat exchangers.

- Tilted Plate:

- Inclined plate at an angle to the horizontal plane, designed to maximize sunlight exposure or direct fluid flow.

## 2. Solar Energy Application

- Vertical Plate: [36]

- Not effective in capturing solar radiation, with a significant drop in performance when the sun is high in the sky.
- Can be utilized in cases where only vertical surfaces can be exploited, such as in building-integrated photovoltaics (BIPVs).

- Tilted Plate: [36]

- Applies in most photovoltaic (PV) solar panel installations.
- Optimum tilt is determined according to latitude and solar angle in winter for optimized energy harvesting.
- Maintains a better performance in direct solar radiation collection.

## 3. Heat Transfer

- Vertical Plate: [37]

- Heat will predominantly pass through convection in a vertical plate.
- Applies in cases where constant convection must occur, such as in radiators.

- Tilted Plate: [37]

- Promotes convective heat transfer; with an inclined position, it can promote or inhibit buoyancy-induced flow, depending on its orientation.
- Possesses a greater variety of convection control.

## 4. Fluid Dynamics

- Vertical Plate: [38]

- Vertical orientation of a plate will produce constant and symmetric flow of a fluid.
- Applies in experiments in wind tunnels in studying drag and lift.

- Tilted Plate: [38]

- Variability in flow dynamics in a tilted plate will introduce fluctuations in the flow, and its attachment, separation, and turbulence will vary with velocity and orientation.
- Applies in inclined sedimentation tanks and in experiments in inclined planes.

## 5. Structural Design

- Tilted Plate:

- Experiences asymmetrical loading with gravity and environment such as wind.
- Needs careful supporting structure to resist bending moments and shear stresses.

- Vertical Plate:

- Symmetric loading with height.
- Easier to support and anchor structurally, with a common use in walls and barriers.

## 6. Applications in Renewable Energy

- Tilted Plate:

- Applied in solar panels, solar water heaters, and mirrors in concentrated solar power (CSP) applications.
- Often dynamically or seasonally adjusted (e.g., tracking systems) for best energy yield.

- Vertical Plate:

- Common in vertical wind turbines and wall mounting for solar panels.
- Often housed in urban environments for optimized space use.

## 7. Aerodynamics:

- Tilted Plate: [39]

- Produces lift or drag, respectively, based on attack plane.
- Central in the shape of airfoils, wings, and inclined planes for studying fluid flow.

- Vertical Plate: [39]

- Maxes out at drag with its orientation perpendicular to flow direction.
- Not the most aerodynamic, but critical in such instances as windbreaks.

**8. Maintenance:**

- Tilted Plate:

- Debris and water can run off through gravity, minimizing maintenance requirements (e.g., in solar panels).

- Vertical Plate:

- Dirt and debris collect in the base sections, and such plates require cleaning at shorter intervals.

**9. Environmental Interaction**

- Tilted Plate:

- Subject to asymmetrical weathering; rain and snow can run off with ease.

- Vertical Plate:

- Equal weathering is experienced down height but less effective at self-cleaning.

**10. Axes Measurement**

- Tilted Plate:

- In a two-dimensional Cartesian coordinate system, a tilted plate covers both the x and y axes since its orientation involves both of the horizontal directions. The plate's tilt creates a projection in the plane of horizontality, and both axes have to be taken into consideration for its measurement. For instance,
- In solar panels, the tilt direction impacts the sunlight exposure of its surface, and such a calculation involves both axes in the plane of x-y.
- In fluid dynamics, tilt alters flow attachment and separation, and measurements in both the horizontal axes become a necessity.
- The tilt orientation ( $\theta$ ) is generally a key variable, with its definition in terms of the horizontal plane.

- Vertical Plate:

- A vertical plate is oriented along the z-axis, perpendicular to the x-y plane. Its single orientation simplifies measurements in terms of height (z-direction). Uses such as heat transfer and wind loading have predominantly considered vertical orientation. Examples include:
- In radiators, computations for heat transfer depend on vertical convection flows in the z-direction.
- In buildings, wind pressure is uniform in direction along height, and z-axis measurements become a necessity. Single orientation simplifies analysis and design when compared to tilted plates.

The following is a comparative analysis between a tilted plate and a vertical plate across various applications:

Aspect	Tilted Plate	Vertical Plate
Orientation	Inclined to horizontal	Perpendicular to horizontal
Solar Efficiency	High (optimized tilt)	Moderate to low
Heat Transfer	Enhanced convection	Constant convection
Fluid Dynamics	Affects flow patterns	Symmetrical flow patterns
Structural Load	Asymmetric, complex	Symmetric, easier to design
Aerodynamics	Variable lift/drag	Maximum drag
Maintenance	Self-cleaning potential	Accumulates debris
Axes Measurement	Measured in x-y axes	Measured in z-axis

TABLE 3.3: Comparison of Vertical and Tilted Plates

### 3.3.4 Experimental Setup

An experimental setup was built to measure the viscoelastic behavior of the fabricated PDMS specimens and some soft tissues, as shown in Figure

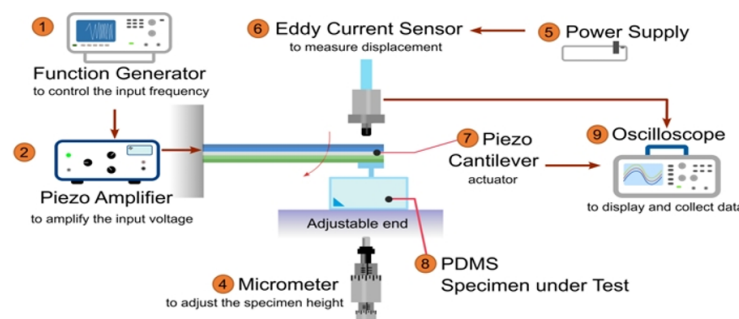


FIGURE 3.10: Experimental Setup

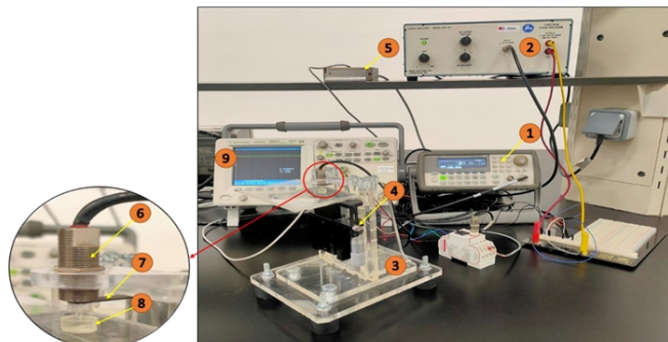


FIGURE 3.11: Experimental Setup

#### I. Setup description

##### 1. Function Generator (1):

- Model: Agilent 33210A
- Purpose: Generates a sinusoidal wave to apply to the piezoelectric cantilever and varies the frequency of the wave.

##### 2. Piezo Amplifier (2):

- Model: EPA-104
  - Purpose: Amplifies the voltage from the function generator to drive the piezoelectric cantilever.
3. **Holding PMMA Structure (3):** Supports the piezoelectric cantilever and helps stabilize the setup.
  4. **Micrometer Stage (4):** Purpose: Accurately adjusts the height of the PDMS specimens and calibrates the piezo actuator and Eddy current sensor.
  5. **Power Supply (5):** Provides the necessary power for the experimental components.
  6. **Eddy Current Sensor (6):**
    - Model: KAMAN KD-2306 – 2S
    - Purpose: Measures the displacement response of the PDMS specimens.
  7. **Piezoelectric Cantilever (7):**
    - Model: T434-A4-201
    - Features: Equipped with a stacked PMMA tip (2 mm diameter, 6 mm height) to focus applied pressure on the PDMS specimens.
  8. **PDMS Specimens (8):** The test samples subjected to pressure from the piezoelectric cantilever tip.
  9. **Oscilloscope (9):**
    - Model: Agilent 5000 – DSO5012A
    - Purpose: Displays and records the input and output signals from the piezo cantilever and Eddy current sensor.

This step-by-step order ensures clarity in describing the experimental setup and its components.

## II. The measuring system holder

A PMMA holder was designed using SolidWorks software. The purpose of the holder is to hold the piezo actuator, the Eddy current sensor, and the micrometer stage as shown in Figure 3.3. To ensure the rigidity of the structure, the main body of the holder was made of PMMA sheet 10 mm thickness. Four rubber legs were attached to the base to reduce the surrounding vibrations and noise. Slots were made in the back of the holder to allow adjusting the micrometer stage to an appropriate location. Two ribs were added to the back to provide more rigidity. An upper cover was added with a suitable slot to carry the Eddy current sensor and to allow adjusting it to the best location above the piezo cantilever free end to give an appropriate output. Besides, a groove was made in the back with suitable dimensions to fix the piezo cantilever properly

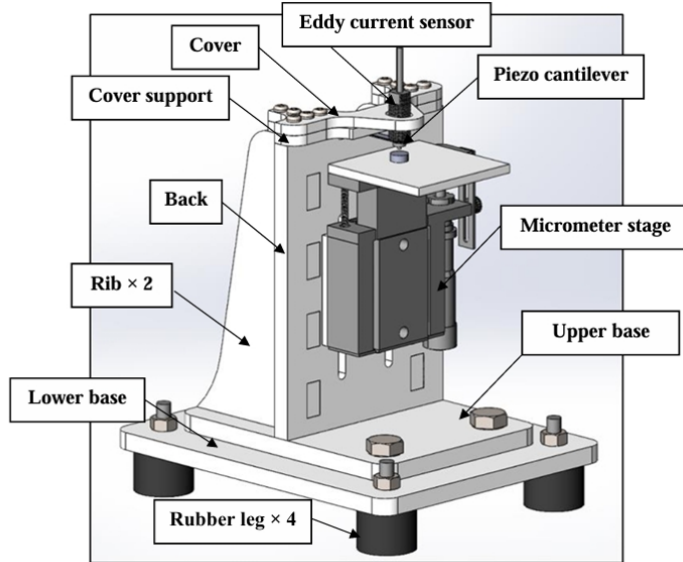


FIGURE 3.12: PMMA Holder

## Experimental Testing

### Silicone Rubber

1. Mixing ratio: 1:1
2. Hardness: 21 Shore A (soft)
3. Temperature resistance:

Up to 200 °C, and for a short time up to 250 °C.

4. It has low viscosity and excellent mechanical properties.
5. It has very high tear resistance in the final consistency and is very flexible.

### Mixing Ratios and Properties

1. Mixing ratios:

D1, D2, D3 are 1 : 5, 1 : 10, 1 : 20 respectively.

2. Hardness: 21 Shore A, damping ratio  $\zeta = \frac{C}{C_c}$ .
3. Damping Ratios:

$\zeta_1, \zeta_2, \zeta_3 = 0.0304, 0.0330, 0.0241$  respectively.

4. For Piezo:

$$\zeta = 0.0311.$$

5. Resonance Frequencies:

- (a) D1: 309.8753,
- (b) D2: 304.9630,
- (c) D3: 304.9630,
- (d) Piezo: 309.8753.

### Silicone Rubber 21 Shore A

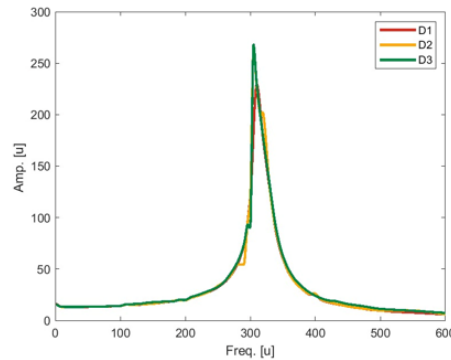


FIGURE 3.13: Results for Silicon 21

#### 1. Mixing ratios:

D1, D2, D4 are 1 : 20, 1 : 30, 1 : 50 respectively.



FIGURE 3.14: Samples of Different Ratios

#### 2. Damping Ratios:

$\zeta_1, \zeta_2, \zeta_4 = 0.076267, 0.077603, 0.080112$  respectively.

#### 3. Resonance Frequencies:

$f_{r1}, f_{r2}, f_{r4} = 370.58, 370.9, 371.02$ .

#### 4. As we notice, there is no significant difference between the three samples at different ratios.

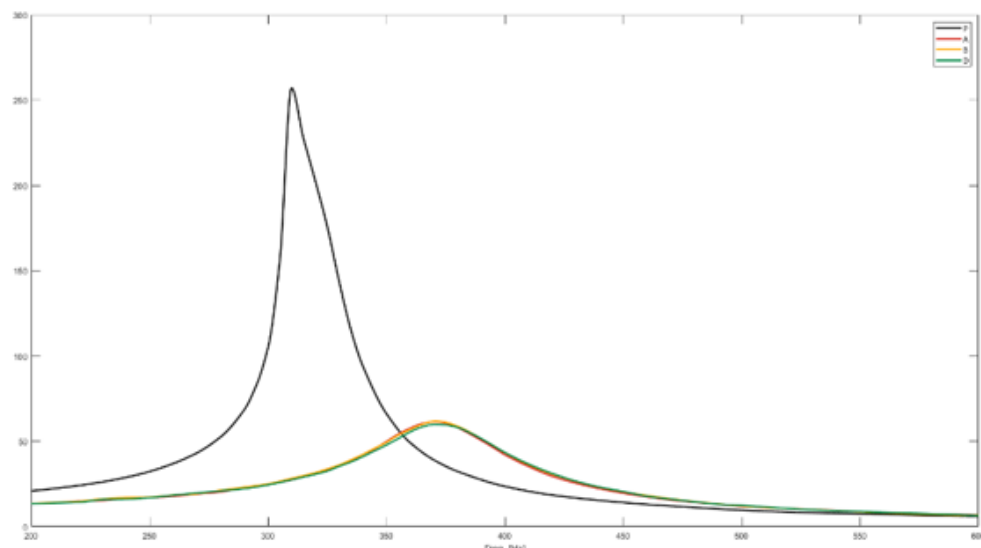


FIGURE 3.15: Result of Samples

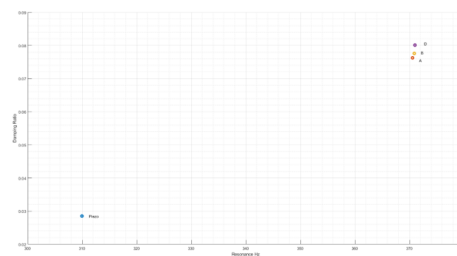


FIGURE 3.16: Result of Samples

## PDMS



FIGURE 3.17: PDM

1. Mixing ratio: 1:45 (1 catalyst to 45 base g).

2. Sample Frequencies and Damping Ratio Responses:

Sample	Zeta ( $\zeta$ )	$f_r$	$f_1$	$f_2$
Piezo	0.027037491	309.9709971	306.8906891	323.6523652
A (1:45)	0.115480831	343.8143814	302.850285	382.2582258

TABLE 3.4: Sample data for Zeta, Resonance Frequency ( $f_r$ ), and Bandwidth Limits ( $f_1, f_2$ ).

- $f_r$ : Resonance frequency.

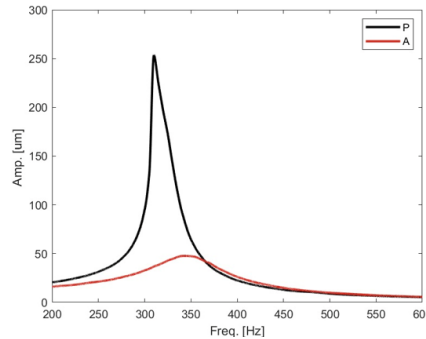


FIGURE 3.18: Resonance Frequency

- Bandwidth:

$$\text{BW}_{\text{Piezo}} = f_2 - f_1 = 323.65 - 306.89 = 16.76 \text{ Hz},$$

$$\text{BW}_{\text{Sample A}} = f_2 - f_1 = 382.26 - 302.85 = 79.41 \text{ Hz}.$$

- Quality Factor ( $Q$ ) indicates the sharpness of resonance:

$$Q_{\text{Piezo}} = \frac{309.97}{16.76} \approx 18.49,$$

$$Q_{\text{Sample A}} = \frac{343.81}{79.41} \approx 4.33.$$

3. Spring Stiffness  $k$ :

$$k = (2\pi f_r)^2 m.$$

4. Temperature Dependence:

$$\Delta f_r \propto -\alpha T.$$

5. PDMS Mixing Ratio: 1:35.

6. Sample Frequencies and Damping Coefficient ( $\zeta$ ) Table:

Sample	Zeta ( $\zeta$ )	$f_r$	$f_1$	$f_2$
A	0.126196869	394.8194819	341.3741374	441.0241024

TABLE 3.5: Sample data for Zeta, Resonance Frequency ( $f_r$ ), and Bandwidth Limits ( $f_1, f_2$ ) for Sample A.

- Quality Factor ( $Q$ ): 3.96,
- Bandwidth: 99.65 Hz.

7. To calculate the density of the material using the formula:

$$f_r = \frac{2}{2\pi} \sqrt{\frac{k}{m}},$$

where:

$$m = \rho \cdot V.$$

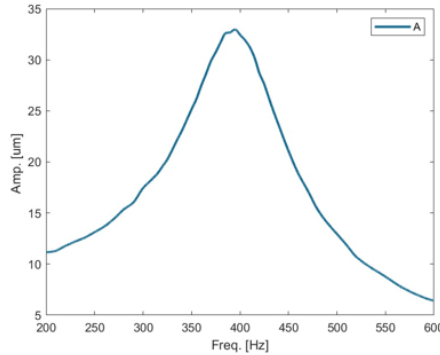


FIGURE 3.19: Results of Sample

## Comparison of S-Shape, Cylinder, and Cone

The following report compares S-shape, cylindrical, and conical geometries in terms of definitions, fluid dynamics, heat transfer, structural loading, usage, aerodynamics, manufacturing, efficiency in use of space, and axes measurement. The relations between such factors have been mentioned, providing a coherent view of the behavior and real-life application of each form.

### 1. Definitions

- **S-Shape:**
  - S-shaped curved form, measured predominantly in the x-y plane.
  - Smooth curvatures in use in structures such as ducts and bridges.
- **Cylinder:**
  - Three-dimensional shape with a circular base and parallel ends extending in the z-axis.
  - Characterized by height ( $h$ ) in the z-axis and radius ( $r$ ) in the x-y plane.
  - Applied in pipes, tanks, and columns.
- **Cone:**
  - Three-dimensional shape with a circular base and a point at an endpoint in the z-axis.

- Characterized by height ( $h$ ), base radius ( $r$ ), and slant height.
- Applied in nozzles, funnels, and chimneys.

## 2. Fluid Dynamics

- **S-Shape:**
  - Incurved path in the x-y plane induces secondary flows and possible vortex.
  - Enhanced mixing but increased resistance and pressure losses.
- **Cylinder:**
  - Interaction occurs between fluid flow and the x-y plane (circumferential flow) and the z-axis (axial flow).
  - Vortex shedding and drag in a direction perpendicular to the axis with an impact on aerodynamic stability.
- **Cone:**
  - Smooth transition in the z-axis of fluid flow, less drag compared to a cylinder.
  - Serves best in acceleration in flow, such as in nozzles and in a diffuser.

## 3. Heat Transfer

- **S-Shape:**
  - Greater heat transfer through mixing and disturbances in flow in the x-y plane.
- **Cylinder:**
  - High surface area for effective transfer in circumferential x-y plane and axial z-axis.
  - Applied in fluid flow parallel and perpendicular to the axis in heat exchangers.
- **Cone:**
  - Gradual taper in the z-axis facilitates controlled heat transfer.
  - Applied in thermal systems with requirements for slow temperature variation.

## 4. Structural Load

- **S-Shape:** [40]
  - Concentrations of stress at curvatures in the x-y plane.
  - Reinforced at bends for loads.
- **Cylinder:** [40]

- Distributed loads uniformly in circumference and length (x-y plane and z-axis).
  - Very stable under radial and axial loads, ideal for pressure vessels.
- **Cone:** [40]
    - Loads transition from the wide base (x-y plane) to the tip via the z-axis.
    - Stable under axial compression.

## 5. Applications

- **S-Shape:**
  - Airfoils (x-y plane curvatures), ducts (smooth path), and bridges (aesthetic and bearing curvatures).
- **Cylinder:**
  - Pipes (z-axis for height, x-y for radius), storage tanks (z-axis for height, x-y for base), wind towers (z-axis).
- **Cone:**
  - Funnels (acceleration of flow along z-axis), chimneys (heat rise along z-axis), nozzles (smooth flow transition).

## 6. Aerodynamics

- **S-Shape:**
  - High drag due to curvatures and secondary flows.
  - Needs to be optimized in an attempt to minimize drag.
- **Cylinder:**
  - High drag coefficient and periodic vortex shedding in cross-flow.
  - Needs aerodynamic damping in structures such as chimneys and towers.
- **Cone:**
  - Very aerodynamic, with its tapered shape.
  - Popular in structures with little drag requirements, such as rockets and wind tunnels.

## 7. Manufacturing

- **S-Shape:** [41]
  - Complicated fabrication with curvatures.
  - Needs specific techniques such as bending and molding.
- **Cylinder:** [41]

- Simple and cheap fabrication via rolling, extrusion, and casting.
- Common in mass production.
- **Cone:** [41]
  - Moderate fabrication complexity, with tapering techniques such as spinning and forming.
  - Precision is key for high-performance use.

## 8. Space Efficiency

- **S-Shape:**
  - Moderate efficiency in terms of space; used when curved forms are applicable.
- **Cylinder:**
  - High efficiency in terms of space for storing and transporting fluids.
- **Cone:**
  - Space-saving for tapered forms, particularly when compact flow regulation is a must.

## 9. Axes and Measurements

- **S-Shape:**
  - Measured in the x-y plane where curvatures form its shape.
- **Cylinder:**
  - Measured in terms of height along the z-axis and in terms of radius in the x-y plane.
- **Cone:**
  - Measured in z-axis (vertical height) and x-y plane (the base radius); and slant height, too.

Aspect	S-Shape	Cylinder	Cone
Orientation	Curved in the x-y plane	Parallel sides along the z-axis	Tapered height along the z-axis
Primary Axes	Measured in x-y plane	Measured in z-axis and x-y	Measured in z-axis and x-y
Fluid Dynamics	Secondary flows in x-y plane	Vortex shedding around x-y plane	Smooth flow along z-axis
Heat Transfer	Enhanced by mixing in x-y plane	High surface area; axial uniformity	Controlled heat transfer along z-axis
Structural Load	Stress at curvature in x-y plane	Uniform distribution along z-axis	Load transition from base to apex
Applications	Ducts, bridges	Pipes, tanks, towers	Nozzles, funnels, chimneys
Aerodynamics	High resistance	High drag	Aerodynamically efficient
Manufacturing	Complex fabrication	Simple fabrication	Moderate fabrication complexity
Space Efficiency	Moderate	High	Compact for tapering designs

TABLE 3.6: Comparison of S-Shape, Cylinder, and Cone Across Various Aspects

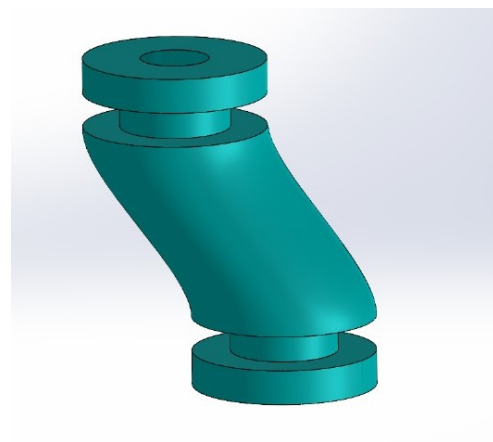


FIGURE 3.20: S-shaped

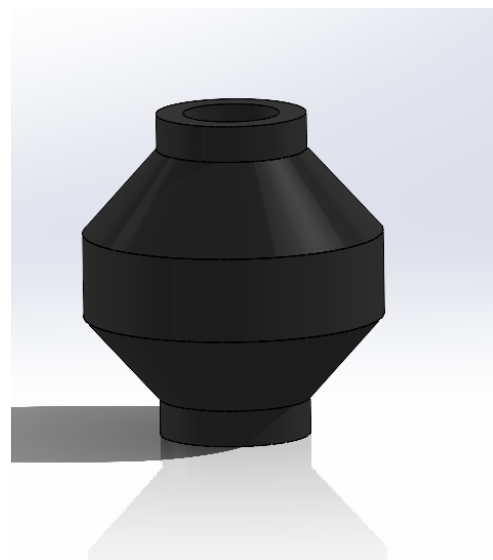


FIGURE 3.21: Conical Form



FIGURE 3.22: Cylindrical Form

## 3.4 Mechanical Design Team

### 3.4.1 Responsibilities of Mechanical Design Team

- Design of gas chamber: Ensure it withstands the operating pressure and prevents leakage.
- Mechanical design: Select proper component mounting techniques for the lens, light source, and PCB-based MEMS sensor to ensure stability.
- Chassis and enclosure: Develop a lightweight chassis and enclosure that balance functionality and aesthetics.
- Sealing solutions: Choose and implement effective sealing techniques at potential leakage points.
- CAD modeling: Create detailed 3D models of all components using SolidWorks, including an assembly model to verify fit, alignment, and space utilization.
- Material and manufacturing selection: Choose suitable materials and fabrication techniques to minimize costs while ensuring proper functionality.
- Testing and validation: Use simulation software such as SolidWorks to conduct tests that verify pressure resistance and structural integrity.
- Certification compliance: Ensure that the device meets ATEX and IP67 certification standards.

### 3.4.2 Component Design and Mounting Techniques

#### Gas Chamber Design

The gas chamber is designed as a cylindrical-shaped chamber with a flange to ensure it withstands the operating gas pressure while maintaining uniform stress distribution. This design maximizes internal volume while minimizing material usage.



FIGURE 3.23: Gas Chamber Design

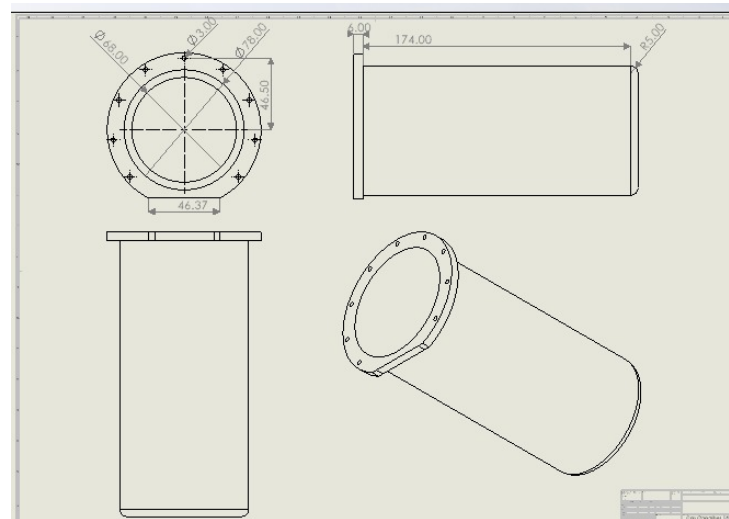


FIGURE 3.24: 2D Drawing of Gas Chamber

The flange allows easy assembly and disassembly, enabling the use of sealing techniques like gaskets and O-rings. An O-ring is placed between the gas chamber and its cover with the following dimensions:

- Inner Diameter: 78mm
- Outer Diameter: 82mm
- Thickness Diameter: 2mm

The groove dimensions in the gas cover are:

- Inner Diameter: 79.56mm
- Outer Diameter: 84.66mm
- Depth: 1.6mm

### Gas Chamber Cover Design

A custom gas chamber cover was designed, considering the placement and mounting of two transparent windows for transmitting light into and out of the chamber.

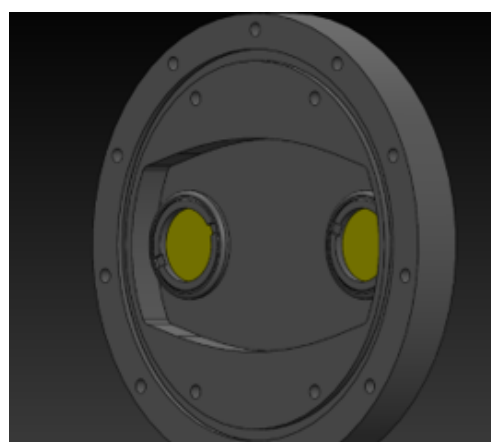


FIGURE 3.25: Gas Chamber Cover

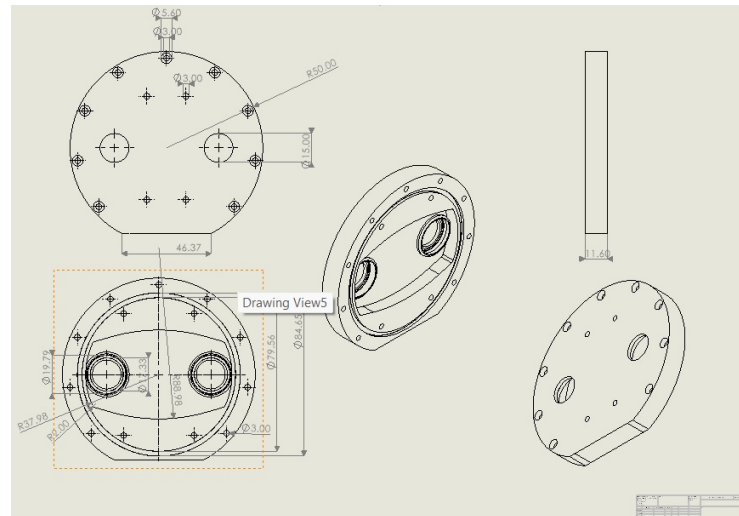


FIGURE 3.26: 2D Drawing of Gas Chamber Cover

The two grooves for the windows are threaded to provide a tight fit using two retaining rings with (M20x0.35) threading. The opening is made using a 19.65mm diameter tap drill.

The chamber cover has nine M3 countersunk screw openings to secure the gas chamber, ensuring high stability and pressure resistance. An O-ring with the following dimensions ensures a tight seal between the mirror and the gas chamber cover:



FIGURE 3.27: Gas Cover Retaining Ring for Mirror

- Inner Diameter: 16.5mm
- Outer Diameter: 18.5mm
- Thickness Diameter: 1mm

Groove dimensions for the O-ring:

- Inner Diameter: 17.325mm
- Outer Diameter: 19.793mm
- Depth: 0.8mm



FIGURE 3.28: Cover Design Closeup

The gas chamber cover is directly connected to the enclosure using four M3 countersunk screws (10mm length) threaded into the front side of the cover.

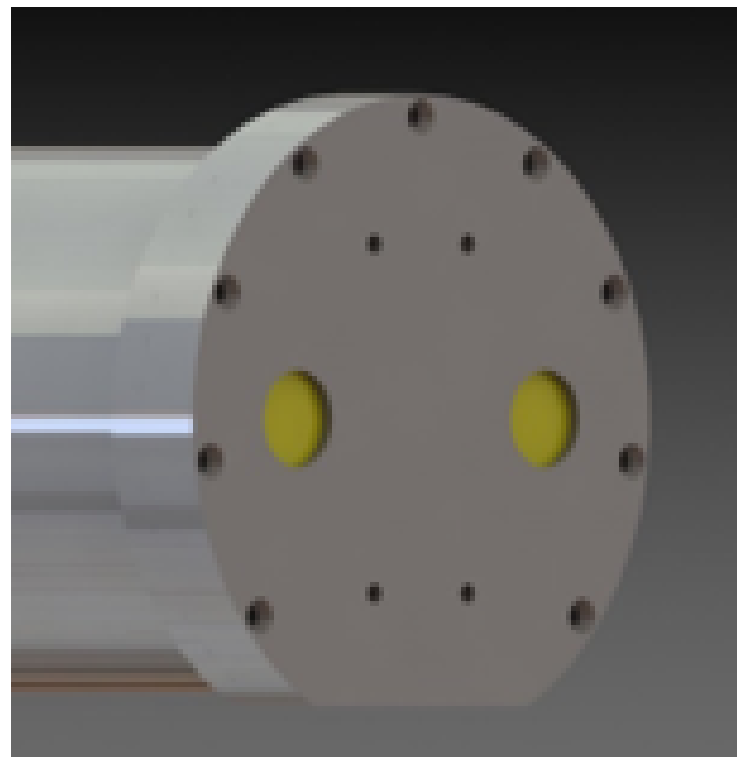


FIGURE 3.29: Chamber with Cover

### Chassis Design

The chassis is a flat sheet with countersink openings at the bottom to mount all components. The openings are M3 countersink openings.

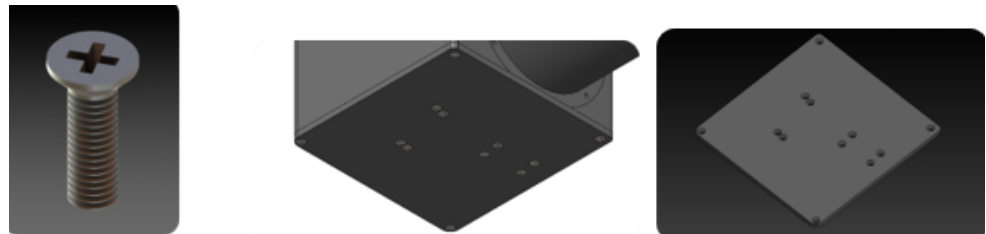


FIGURE 3.30: Chassis Screws

### Light Source Mount Design

A custom design ensures stability and a secure fit.

- Four openings at the top accommodate hex head nut screws of M2-0.4 size, with a thread length of 3.6mm and a total length of 4mm.
- Four openings at the bottom accommodate M3 countersunk screws for mounting to the chassis.

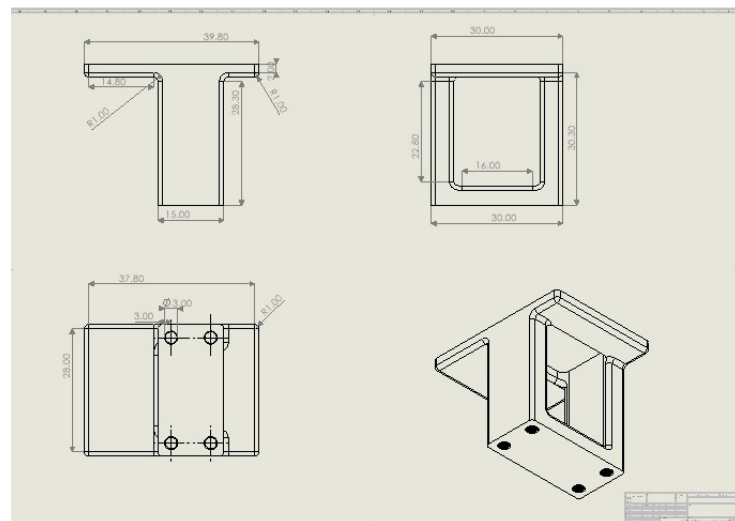


FIGURE 3.31: 2D Drawing of Light Source Mount



FIGURE 3.32: Light Mount Design

### Lens Mount Design

A custom-designed lens mount uses retaining rings to ensure a firm mounting and prevent movement due to vibrations or clearance issues. The retaining rings are commercially available from Thorlabs.

- The lens mount and retaining rings have (M12.5 x 0.5) threading.
- Clear aperture: 10.2mm.
- The retaining rings feature spanner wrench slots compatible with the SPW801 spanner wrench from Thorlabs.
- Two openings at the bottom are threaded for M3 countersunk screws for chassis fixation.



FIGURE 3.33: Lens Fixation Design

#### 3.4.3 Pump Selection

The Parker BTX B1C-090P24AN-03 miniature diaphragm pump was chosen for its key features:



FIGURE 3.34: BTX B1C-090P24AN-03 miniature diaphragm pump

- Maximum pressure: 1.79 bar (higher than the required 1.5 bar).
- Compact size: 56.5mm × 30mm, lightweight (125g).
- Brushless DC motor with a service life of up to 15,000 hours.
- Low vibration and noise level (<45 dB).
- Flow rate up to 5.5 L/min with PWM speed control.
- Chemical-resistant materials suitable for most gases.

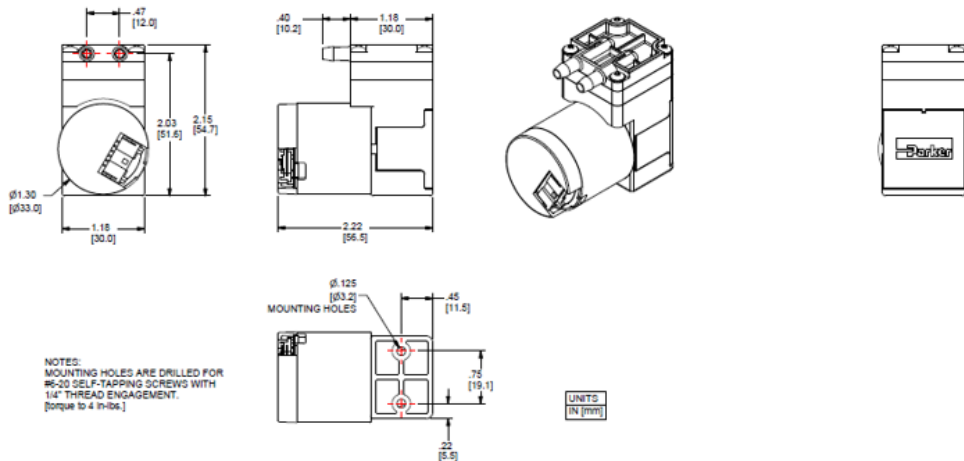


FIGURE 3.35: Pump Design

### Hose, Hose Clamps, and Quick Connectors

For our system, we selected a \*\*1/8" (3.2mm) ID Nitrile Fuel Hose\*\*, which can support up to 8.6 bar pressure and withstand temperatures from -40°C to +125°C. The hose is secured using \*\*stainless steel mini hose clamps (2.5-8mm diameter range)\*\* for leak-free connections.



FIGURE 3.36: Hose

Quick and easy connections can be made by using Nitto Kohki MC-10SM Micro Cupla SM-Type Coupling threaded push-to-connect quick connectors, rated for up to 15 bar pressure. Installation shall be done in two places: at the inlet for the gas from the outer atmosphere that is threaded in the enclosure, and at the inlet of the gas chamber cover.

This design-suggested quick connector is Atex and IP67 compliance. To provide a gas outlet from the chamber, we suggest another MICRO CUPLA connector inside of the chamber for controlled gas release and possible recirculation or analysis.

The installation will involve threading the M10 CUPLA connectors into appropriate openings in the enclosure, chamber cover, and pump, and attaching the hose onto the barbed ends of connectors by securing with the hose clamps.

Also the use of thread sealant (Loctite 577 for example) for stronger sealing. This will provide a reliable, leak-proof, and easily maintainable gas delivery

system that will meet our pressure requirements and will facilitate both gas input and output for the sensor chamber. So, the gas path will be as follows:

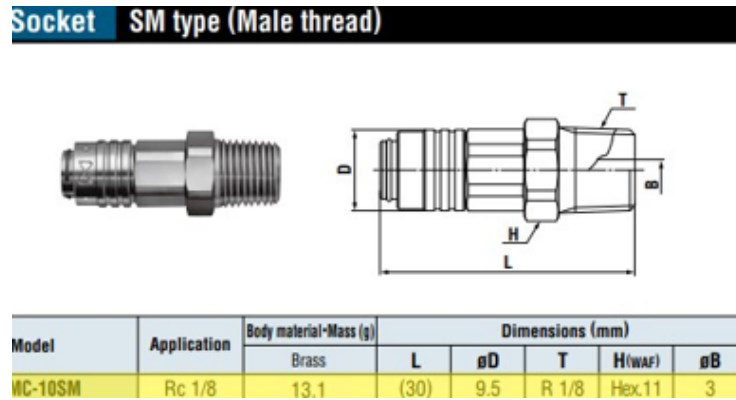


FIGURE 3.37: Male Socket

It is sucked into an M10 Threaded opening in the enclosure which has a quick connector connected in it, then it will go into the hose and then inside the pump. After the pump pressurizes the gas it will go from its outlet through the hose into the quick connector threaded in the gas chamber cover. At the other end of the gas chamber there will be another quick connector which is responsible for acting as the outlet of gas from the gas chamber.

### 3.4.4 PCB Sensor Mount

A custom sensor mount was designed. The sensor PCB is secured using \*\*M2.5 hex flange head tapping screws (16mm thread length)\*\* with spacers to ensure proper airflow and component clearance.



FIGURE 3.38: Sensor Mount

- The mounting part is attached to the chassis using M3 countersunk screws.
- Pre-machined openings at the bottom ensure flush fitting.
- Side openings allow fixation of the PCB.

This mounting technique was decided upon because it gives stability to the design, is easy to assemble, and is modular in design. These spacers will maintain electrical isolation and eliminate any mechanical stress on the PCB.

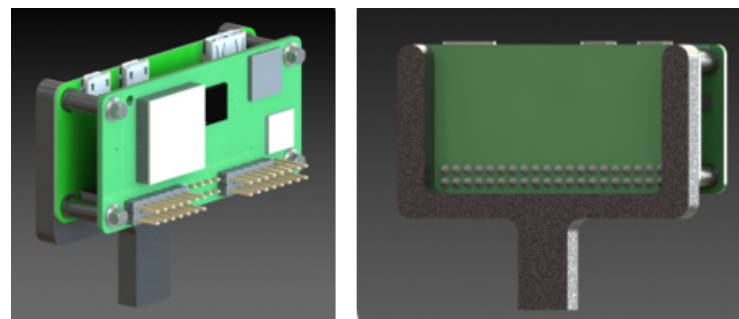


FIGURE 3.39: PCB Mounted

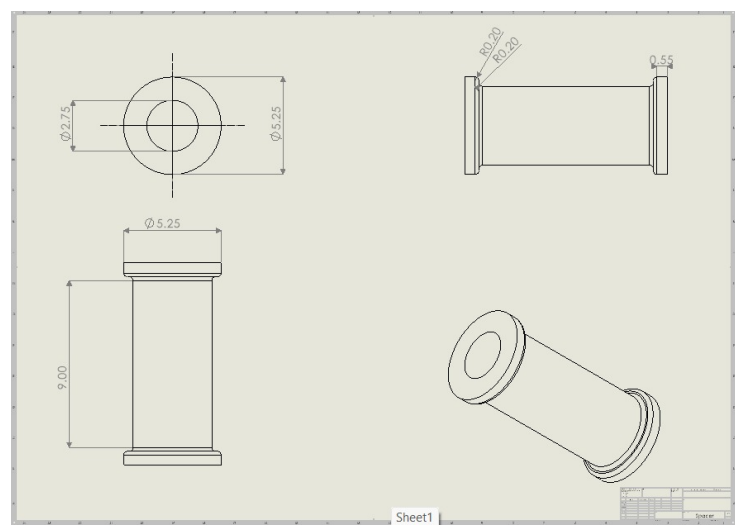


FIGURE 3.40: 2D Drawing of PCB Spacers

### 3.4.5 Final Assembly

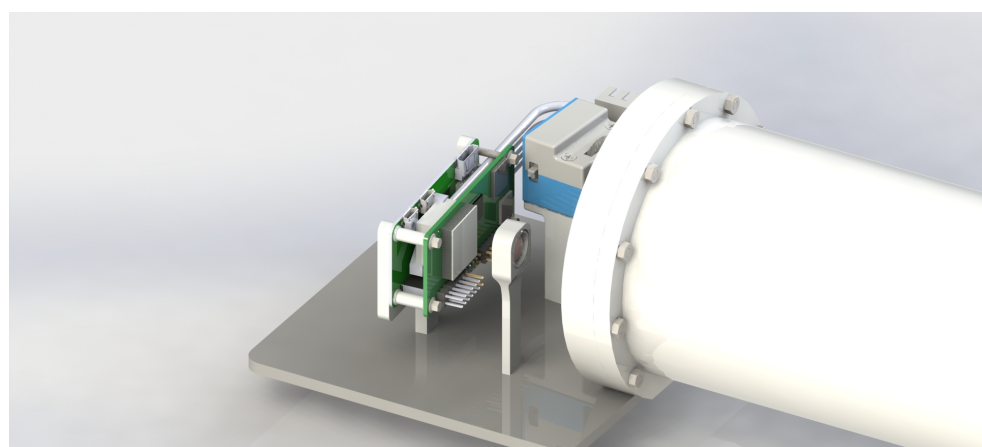


FIGURE 3.41: Final Assembly

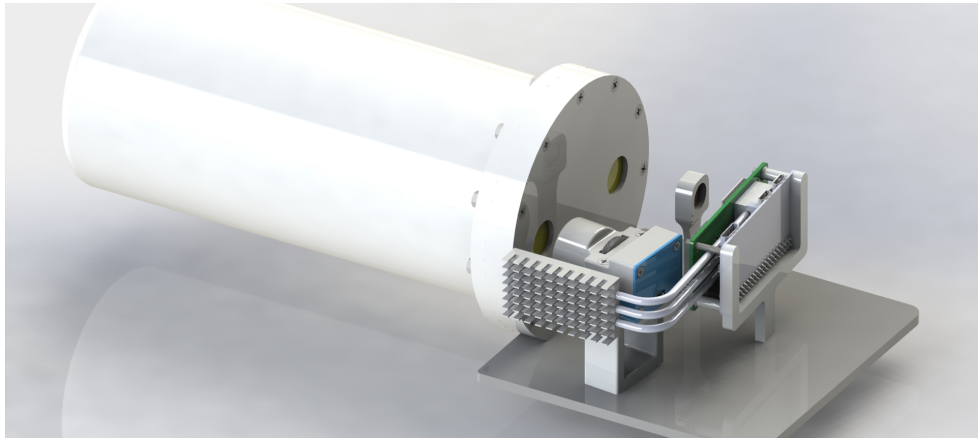


FIGURE 3.42: Final Assembly

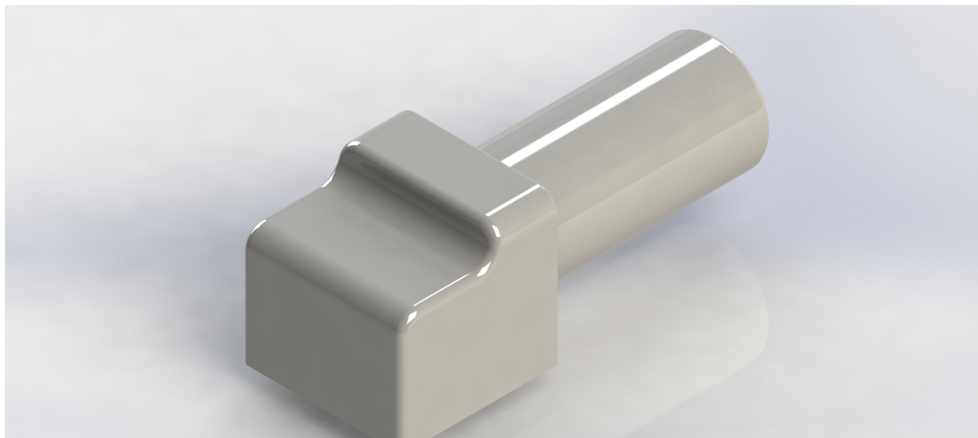


FIGURE 3.43: Full Sensor Body

### 3.4.6 Material Selection

Glass Reinforced Plastic (GRP) was selected as the primary material for the device due to its superior mechanical and chemical properties, which align with the project's operational requirements. GRP offers an excellent strength-to-weight ratio, ensuring structural integrity while maintaining a lightweight design capable of withstanding an operational pressure of 1.5 bar. Its high chemical resistance allows for the containment of various gases without the risk of degradation or reactivity. Additionally, GRP exhibits low thermal conductivity, which is crucial for maintaining stable internal temperatures, thereby enhancing the accuracy of gas measurements.

From a safety perspective, GRP is non-conductive and non-sparking, making it compliant with ATEX certification requirements for operation in potentially explosive environments. The material's moldability facilitates the seamless integration of the cylindrical gas chamber, lens mounts, and other structural components into a unified design. Furthermore, GRP's hardness and environmental resistance contribute significantly to achieving an IP67 rating, ensuring protection against dust and water ingress. The combination of these properties enhances the overall performance, safety, and durability of the device.

## Chapter 4

# Results

### 4.1 Thermal Management Team:

In this research a thermoelectric cooler (TEC) from Laird Thermal Systems and this TEC model name is PCX4-7-F1-2020-TA-RT-W6 which is a TEC from the PowerCycling PCX Series. [42]

#### 4.1.1 Model Specification:

Hot Side Temperature	27.0 °C	50.0 °C	80.0 °C
Qcmax (T = 0)	19.4 Watts	20.9 Watts	22.4 Watts
Tmax (Qc = 0)	73.6 °C	82.6 °C	93.1 °C
I <sub>max</sub>    (@ Tmax)	4.0 Amps	3.9 Amps	3.8 Amps
V <sub>max</sub> (V @ Tmax)	8.3 Volts	9.2 Volts	10.4 Volts
Module Resistance	1.94 Ohms	2.18 Ohms	2.50 Ohms
Max Operating Temperature	120 °C		
Weight	9.0 gram(s)		

TABLE 4.1: Thermal and Electrical Characteristics at Different Hot Side Temperatures

This table is used to calculate the parameters that have been mentioned before:  $\alpha_m$ ,  $\Theta_m$ , and  $R_m$ .

#### Electrical Resistance $R_m$

$R_m$  is calculated using the formula:

$$R_m = \frac{V_{\max}}{I_{\max}} \times \frac{(T_h - \Delta T_{\max})}{T_h} \quad \Omega$$

From the table:

- $T_h = 27^\circ C$
- $\Delta T_{\max} = 73.6^\circ C$
- $V_{\max} = 8.3$  Volts
- $I_{\max} = 4.0$  Amps

Therefore:

$$R_m = 1.56 \quad \Omega$$

### Thermal Resistance $\Theta_m$

Thermal resistance  $\Theta_m$  is given by:

$$\Theta_m = \frac{\Delta T_{\max}}{I_{\max} V_{\max}} \cdot \frac{2T_h}{(T_h - \Delta T_{\max})} \left[ \frac{\text{K}}{\text{W}} \right] \quad (4.1)$$

$$\Theta_m = 5.87 \text{ K/W}$$

### Seebeck Coefficient $\alpha_m$

The Seebeck coefficient  $\alpha_m$  is calculated as:

$$\alpha_m = \frac{V_{\max}}{T_h} \left[ \frac{\text{V}}{\text{K}} \right] \quad (4.2)$$

$$\alpha_m = 0.027 \text{ V/K}$$

#### 4.1.2 The Circuit:

After calculating the 3 parameters they will be used in LTspice as parameters for the circuit to see if it will match the data from the datasheet. The Model that will be used in LTspice is an equivalent circuit to the theoretical circuit mentioned earlier.

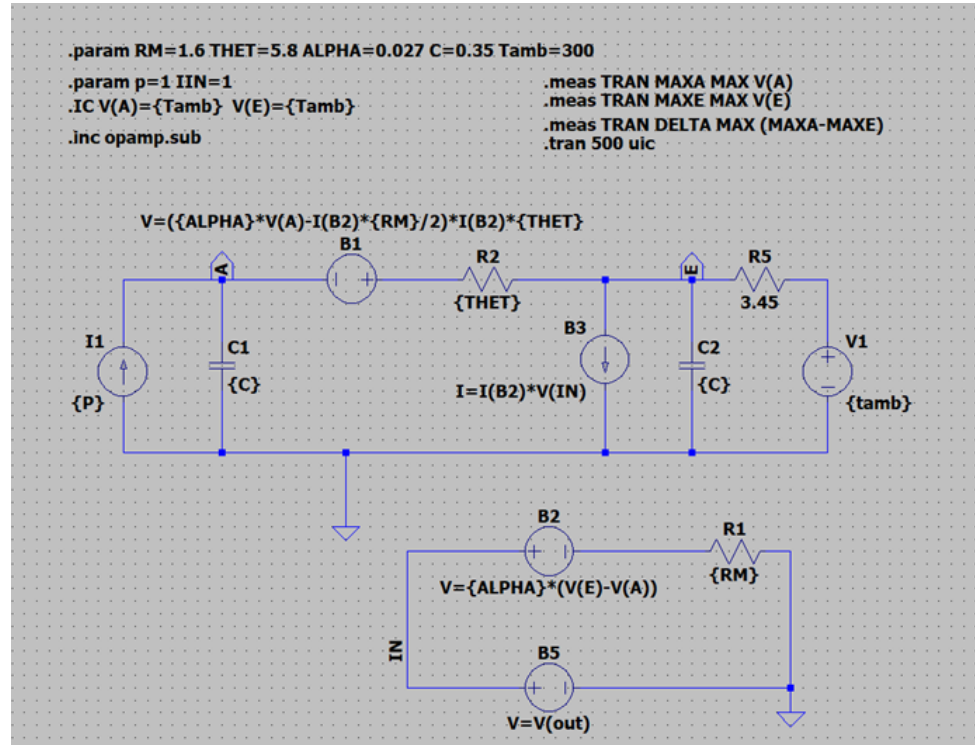


FIGURE 4.1: Circuit Design on LTspice

## List of Functions

- **.param:** A function used to define variables and parameters.
  - $R_m$  is defined as RM.
  - $\Theta_m$  is defined as THET.
  - $\alpha_m$  is defined as ALPHA.
  - $C = 0.35$  is the value of every capacitor used in the circuit, assigned the value C.
  - $P$  is the value of the current source I1 and represents the operating current.
  - $T_{amb} = 300$  K, which corresponds to  $T_h = 27^\circ\text{C}$  (converted as  $27 + 273$ ).
- **.IC:** Specifies the initial condition for Point A and Point E with the  $T_{amb}$  value.
- **.meas:** A measure function used to generate a table with a list of points in the graph.
- **.Tran:** Defines how to run or simulate the circuit.
- **.inc:** An include function used to include a library.

### Seebeck Effect Circuit:

This is the Circuit that mainly plays an important role in the Peltier effect and will be explained later why but this circuit is for the Seebeck effect value, and it is attached to the electrical resistance  $R_m$  and the output of this circuit will be input for other dependent source.

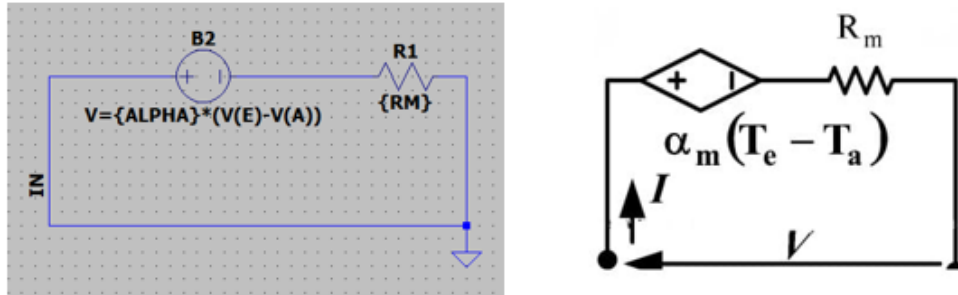


FIGURE 4.2: Seebeck Effect Circuit

### The Main Circuit:

This circuit consists of two main sources:

1. **Voltage Source B1:** A voltage-dependent source that takes input from the output of the Seebeck Effect circuit. The voltage source follows the equation as shown in the figure.
2. **Current Source B3:** A current-dependent source representing the power dissipated by the electrical circuit. This dissipation is considered waste heat that must be removed from the hot side.

3. **Current Source I1:** The operating current of the circuit, which determines the circuit's operational characteristics based on the model used.
4. **Voltage Source V1:** A voltage source that represents  $T_{amb}$ , marking the starting temperature of the hot side. This ensures the flow starts from the right side to the left side.
5. **Point E and Point A:** These are the two measurement points before and after the Peltier effect in the model. Point E is the starting point, and Point A is the ending point.
6. **Resistor R2:** Represents  $\Theta_m$ , the thermal resistance of the model.
7. **Resistor R5:** The total resistance of the heatsink, heat pipes, and the overall cooling system.

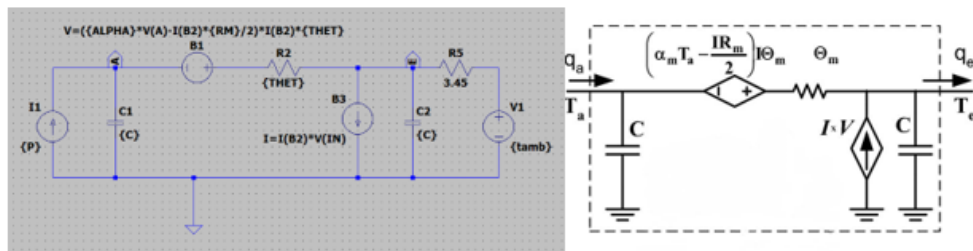


FIGURE 4.3: Main Circuit

#### 4.1.3 The Simulation:

After adding all the parameters of the model and the design in the circuit, the simulation should provide if the model is correct or not by comparing the results of the simulation to the results of the datasheet of the model. First trial: it was at operating current 1 Amp and Tamb 300 (constant at all trials) and the simulations were transient.

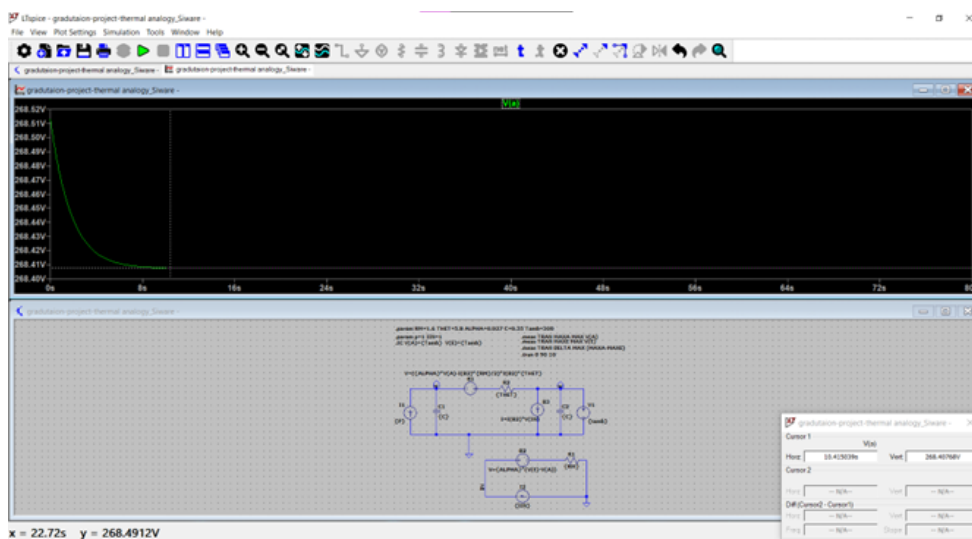


FIGURE 4.4: Simulation Graph 1

## Simulation Results

After the simulation, the expected or theoretical value (calculated from  $Q = \frac{\Delta T}{\theta_m}$ ) at Point A was  $-6.1^\circ\text{C}$ . However, as shown in the figure, the actual value was  $268.4^\circ\text{K}$ , which is close to  $-5^\circ\text{C}$ .

The difference or error arises due to several factors, including:

- Ignored resistances such as heat pipes, heat sinks, etc.
- The circuit currently lacks a feedback control system, meaning it operates as an open-loop system.

To further analyze the system behavior, the operating current was gradually increased while running a DC sweep to display all possible values.

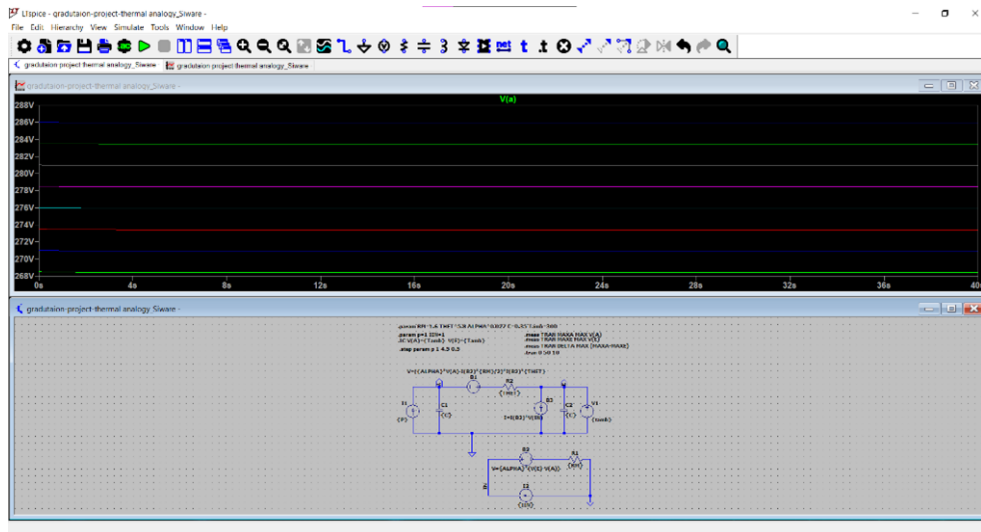


FIGURE 4.5: Enter Caption

All these different currents from 1 to 4.5 ( $I_{max}$ ) with incrementing 0.5 Amps prove that the model matches the Data sheet, and the model is theoretically correct, this is also later proved to match real life calculations.

### Datasheet:

While working at  $Q = 33.17 \text{ W}$  used to know from the operating current if it matches the model.

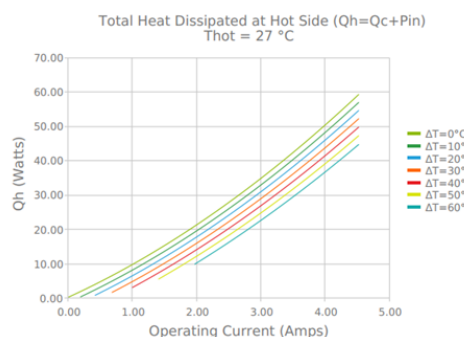


FIGURE 4.6:  $Q_h$  vs Operating Current Graph

The problem here is that there is a change in the simulation to the data sheet, but these errors aren't significant and are acceptable. To minimize the error as much as possible the loop of the circuit should be closed with feedback and to make a controller.

### Closed Loop Circuit:

This is the circuit that will minimize the error of the circuit and make its value much closer to the datasheet and the desired values.

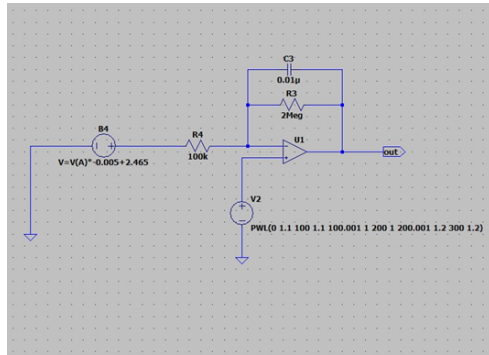


FIGURE 4.7: Closed Loop Circuit

This is the control circuit that consists of 2 voltage sources and 1 universal op-amp and the output of this circuit is used to be an input for the Seebeck effect to change the value of the signal of the output of the Peltier effect to be more accurate through inputting the signal of the control circuit to the voltage source B5.

This is the control signal through  $V(\text{out})$ , or the port named out.

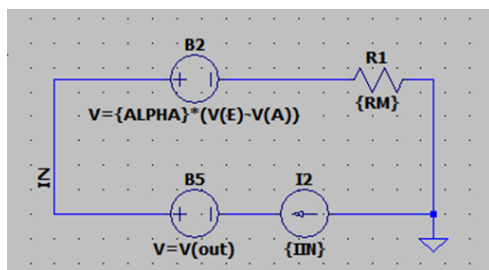


FIGURE 4.8: Output Circuit

There was an enormous difference with better and closer values to the datasheet shown below, after successfully closing the loop using a feedback signal.

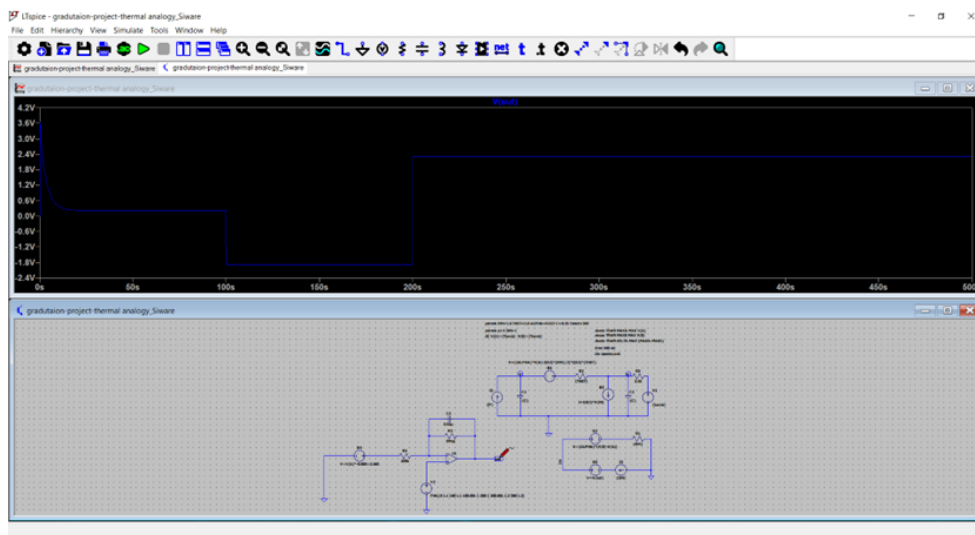


FIGURE 4.9: Closed Loop Results

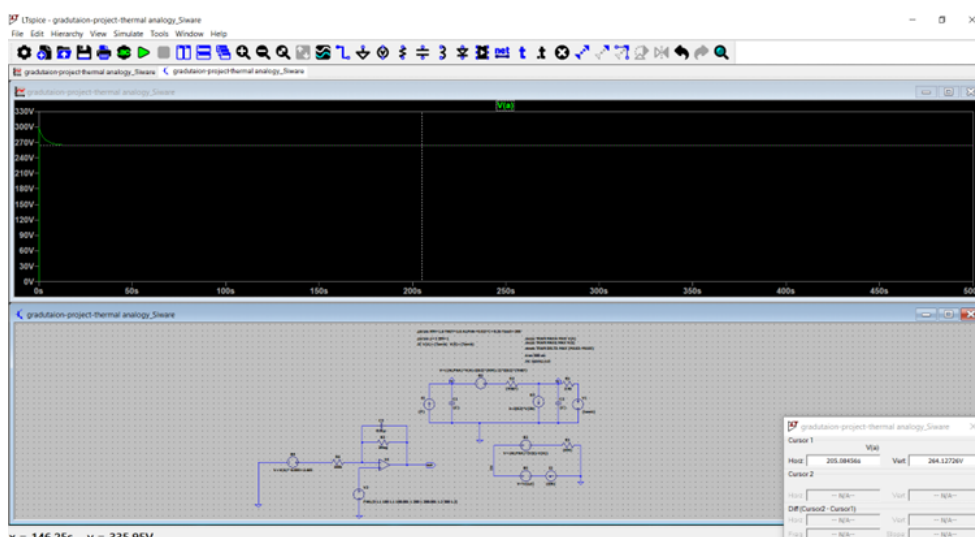


FIGURE 4.10: Closed Loop Results 2

By similarity in the Circuit and sweeping the current to show all the possible values for the Peltier model from the minimum value to the maximum value.

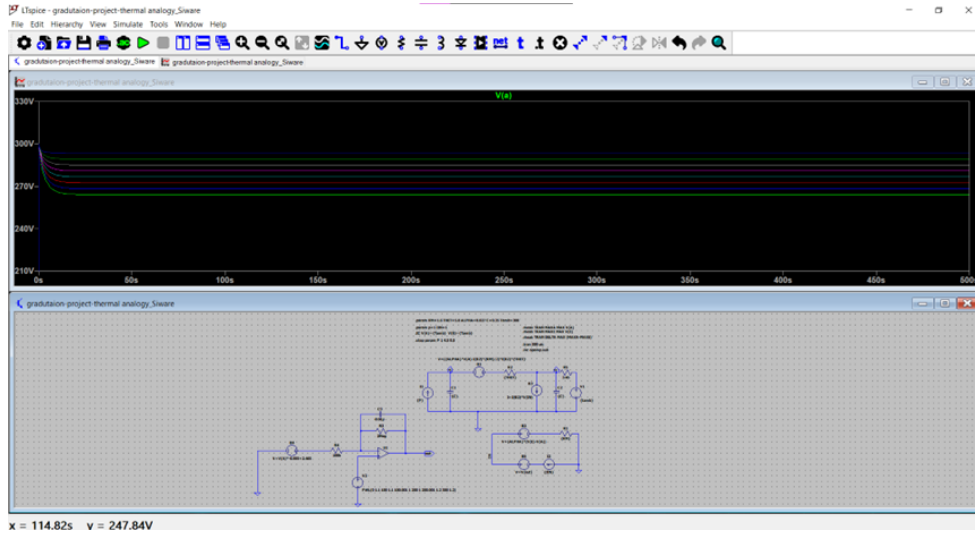


FIGURE 4.11: Results of Peltier Temperatures

### Important Notes:

The op-amp cannot handle the high signal of 300 V so we use the Resistor 2Meg to minimize this value as much as possible so that the op-amp could invert the signal to the control signal. To make the controller perform better the constants in B4 could be changed and tuned until it reaches the desired values.

### Derivation of the Transfer Function

The transfer function describes the relationship between the temperature variation  $\Delta T_{ac}$  and the voltage variation  $V_{ac}$  in the system. The derivation is based on the following steps:

#### Basic Equations

##### 1. Heat Flow:

$$\begin{aligned} q_a &= \frac{\Delta T}{\Theta_m} + \alpha_m T_a I - \frac{I^2 R_m}{2} \\ q_e &= \frac{\Delta T}{\Theta_m} + \alpha_m T_e I + \frac{I^2 R_m}{2} \end{aligned}$$

##### 2. Electrical Equation:

$$V = \alpha_m \Delta T + IR_m$$

##### 3. Rate of Change of Temperature:

$$C \frac{d(\Delta T)}{dt} = q_a - q_e$$

### Linearization (Small Signal Analysis)

For small signal analysis, variations are represented as:

$$\Delta T = \Delta T_0 + \Delta T_{ac}, \quad V = V_0 + V_{ac}, \quad I = I_0 + I_{ac}$$

The linearized equations become:

$$V_{ac} = \alpha_m \Delta T_{ac} + I_{ac} R_m$$

#### 2. Heat Flow:

$$q_{a,ac} - q_{e,ac} = \frac{\Delta T_{ac}}{\Theta_m} + \alpha_m I_0 \Delta T_{ac}$$

#### 3. Rate of Change of Temperature:

$$C \frac{d(\Delta T_{ac})}{dt} = \frac{\Delta T_{ac}}{\Theta_m} + \alpha_m I_0 \Delta T_{ac}$$

### Laplace Transform

Using the Laplace transform:

$$Cs\Delta T_{ac}(S) = \frac{\Delta T_{ac}(S)}{\Theta_m} + \alpha_m I_0 \Delta T_{ac}(S)$$

Rearranging:

$$\Delta T_{ac}(S) \left( Cs - \frac{1}{\Theta_m} - \alpha_m I_0 \right) = 0$$

Defining the time constant  $\tau$ :

$$\tau = \frac{C}{\frac{1}{\Theta_m} + \alpha_m I_0}$$

The resulting equation:

$$\Delta T_{ac}(S) = \frac{1}{1 + \tau S}$$

### Final Transfer Function

Combining the equations, the transfer function  $H(S)$  is:

$$H(S) = \frac{\Delta T_{ac}}{V_{ac}} = \frac{\alpha_m / R_m}{1 + \tau S}$$

Given the parameter values:

$$\alpha_m = 0.027 \text{ V/K}, R_m = 1.6 \Omega, \Theta_m = 5.8 \text{ K/W}, C = 0.35 \text{ J/K}, I_0 = 4.5 \text{ A}$$

The time constant  $\tau$  is:

$$\tau = 1.755 \text{ s}$$

The final transfer function:

$$H(S) = \frac{0.016875}{1 + \tau S}$$

#### 4.1.4 Heat Dissipation System Calculations

In this section, we present the detailed thermal resistance calculations and overall performance evaluation of the designed heat dissipation system.

##### Thermal Resistance of the Heat Sink:

- The thermal resistance of the heat sink depends on its material, dimensions, and convection conditions. Given:
  - Heat sink material: Aluminum (thermal conductivity  $k = 205 \text{ W/mK}$ )
  - Base dimensions: Length  $L = 0.04425 \text{ m}$ , Width  $W = 0.024 \text{ m}$ , Thickness  $t = 0.004 \text{ m}$
  - Natural convection condition (thermal resistance at the fins):  $R_{\text{fins}} = 2.55 \frac{\text{°C}}{\text{W}}$
- Formula for base thermal resistance:

$$R_{\text{base}} = \frac{t}{k \cdot L \cdot W}$$

- Substitution:

$$R_{\text{base}} = \frac{0.004}{205 \cdot 0.04425 \cdot 0.024} = 0.018 \frac{\text{°C}}{\text{W}}$$

- Total thermal resistance of the heat sink (base + fins):

$$R_{\text{sink}} = R_{\text{base}} + R_{\text{fins}} = 0.017 + 2.55 = 2.55 \frac{\text{°C}}{\text{W}}$$

- Final value matches the provided value.

##### Thermal Resistance of Heat Pipes:

- Resistance of a single heat pipe:  $R_{\text{single}}$
- For parallel heat pipes:

$$\frac{1}{R_{\text{pipes}}} = \frac{1}{R_{\text{single}}} + \frac{1}{R_{\text{single}}} + \frac{1}{R_{\text{single}}}$$

- So finding the thermal resistance of one heat pipe, from the datasheet or by calculations would yield the total heat pipes resistance:

$$R_{\text{pipes}} = 0.0278 \frac{\text{°C}}{\text{W}}$$

- **Thermal Resistance of Thermal Paste:**

- A commercially available thermal paste (e.g., HY883 model from Halnziye Electronics) was used, with:
  - \* Thermal conductivity:  $k = 6.5 \text{ W/mK}$
  - \* Thickness:  $L = 0.0012 \text{ m}$

\* Cross-sectional area:  $A = 0.0004 \text{ m}^2$

- Formula:

$$R_{\text{paste}} = \frac{L}{k \cdot A}$$

- Substitution:

$$R_{\text{paste}} = \frac{0.0012}{6.5 \cdot 0.0004} = 0.461 \frac{\text{°C}}{\text{W}}$$

- **Thermal Resistance of the Thermal Via Array:**

- The thermal resistance of the via array was calculated using the ProtoExpress Thermal Via Calculator [22] as:

$$R_{\text{via}} = 0.1286 \frac{\text{°C}}{\text{W}}$$

- **Total Thermal Resistance:**

- Summing up all resistances:

$$R_{\text{total}} = R_{\text{via}} + R_{\text{paste}} + R_{\text{TIM}} + R_{\text{pipes}} + R_{\text{sink}}$$

- Substitution:

$$R_{\text{total}} = 0.1286 + 0.461 + 0.27 + 0.0278 + 2.57 = 3.457 \frac{\text{°C}}{\text{W}}$$

### Calculation of Hot Side Temperature, $T_h$

The hot side temperature is determined using the equation:

$$Q_h = \frac{\Delta T}{R_{\text{total}}}, \quad \Delta T = T_h - T_c$$

Given:

- $Q_h = 5.72 \text{ W}$
- $T_c = 27 \text{ °C}$
- $R_{\text{total}} = 3.4344 \frac{\text{°C}}{\text{W}}$

Substituting:

$$\Delta T = Q_h \cdot R_{\text{total}} = 5.72 \cdot 3.4344 = 19.64 \text{ °C}$$

$$T_h = T_c + \Delta T = 27 + 19.64 = 46.77 \text{ °C}$$

### Heat Loads, $Q_h$ and $Q_c$

The heat loads such as  $Q_c$  was given by Si ware electronics, this is the expected heat load from the laser and electronics, and it is equal to 5W, this is the amount of heat that the cold side of the TEC has to absorb to prevent the sensor from heating and to keep it at a constant temperature of 27°C, from this value finding the  $Q_h$  was simple, it is the the  $Q_c + I * V$  where I and V are the operating currents and voltages respectively. Therefore the

needed values are the operating current and voltages which can simply be found from the datasheet of the TEC used in this research. [42]

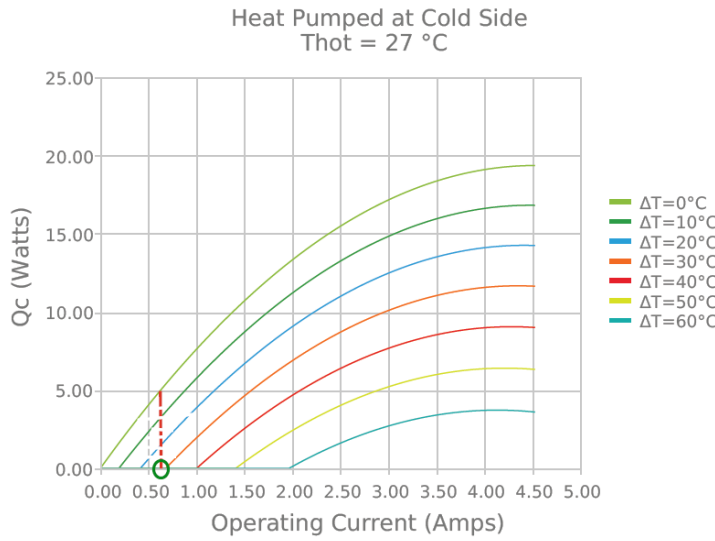


FIGURE 4.12: Operating Current Graph

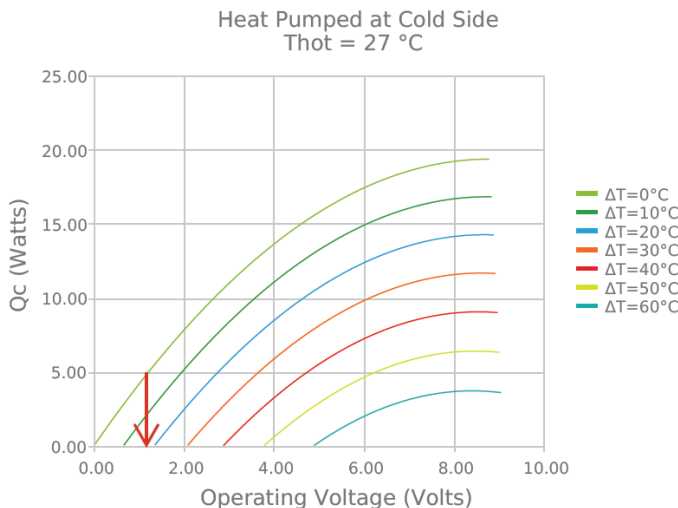


FIGURE 4.13: Operating Voltage Graph

For both the operating voltage and current values the values were taken at an assumption that at time = 0 both  $T_h$  and  $T_c$  are the same therefore delta T is zero.

### System Performance Evaluation

The results confirm that the thermal resistance calculations align with the provided data. The total thermal resistance ensures the hot side temperature remains below 50°C, validating the system's design. Further optimization of thermal paste or active cooling options could improve performance.

## 4.2 Vibration Team Results

### Numerical Simulation Using Finite Element Analysis (FEA)

Finite element analysis (FEA) is a powerful computational method used in engineering systems to analyze dynamic properties. This approach allows engineers to identify the natural frequencies and mode shapes of a system, facilitating early detection and prevention of potential problems such as resonances resulting from these frequencies. Finite element analysis provides an intuitive means of optimizing design parameters, ensuring that systems operate efficiently under varying load conditions [43].

#### Material Properties for Vibration Isolator Damper Analysis Using ANSYS:

In this study, two main materials were selected for the analysis of vibration isolators: PDMS (Sylgard™ 184 Silicone Elastomer) and acrylic (PMMA). These materials were selected based on their distinctive mechanical and thermal properties, which significantly affect the performance of vibration isolators under dynamic loading conditions.

#### Material Properties for Vibration Isolator Damper Analysis Using ANSYS

##### 1) PDMS (Sylgard™ 184 Silicone Elastomer)

- **Density:** 1.03 g/cm<sup>3</sup>
- **Young's Modulus:** 0.05 MPa
- **Poisson Ratio:** 0.47
- **Tensile Strength:** 980 psi (6.7 MPa)
- **Coefficient of Thermal Expansion:** 340 ppm/°C
- **Thermal Conductivity:** 0.15 W/m·K
- **Damping Ratio (1:45):** 0.1154808

PDMS's low Young's modulus means it is highly elastic, making it an ideal material for absorbing vibration. However, its high coefficient of thermal expansion means that PDMS is sensitive to temperature changes, resulting in dimensional variations. This must be carefully considered during the design phase to ensure the stability of the vibration isolator. Additionally, PDMS has a relatively low thermal conductivity, making it suitable for applications that require thermal insulation [44].

PDMS is also widely used in electronic packaging due to its excellent insulating properties and flame resistance. Its ability to be cured at room temperature or with heat makes it versatile for a variety of industrial applications, including vibration isolation in drones. [45]

##### 2) Acrylic (PMMA)

- **Density:** 1180 kg/m<sup>3</sup>
- **Young's Modulus:** 2.7 GPa

- **Poisson Ratio:** 0.4
- **Tensile Strength:** 65 MPa
- **Compressive Strength:** 100 MPa
- **Coefficient of Thermal Expansion:** 70 ppm/ $^{\circ}$ C
- **Thermal Conductivity:** 0.19 W/m·K

Unlike PDMS, PMMA is a stiffer material due to its higher Young's modulus. This makes it suitable for applications that require structural integrity and rigidity. However, PMMA has a lower damping capacity compared to PDMS, making it less effective at absorbing vibrations.

### System Analysis

To analyze the dynamic behavior of the vibration isolator, simulations were performed using data collected from two different UAVs: the DJI Matrice 100 and the DJI Matrice 600 Pro. The purpose of this analysis was to evaluate the performance of the vibration isolator under real-world operating conditions, taking into account the random vibrations generated by the UAV during flight. The vibration data for these UAVs were obtained from a study on the vibration characteristics of UAVs, which provided detailed power spectral density (PSD) data for analysis. [37]

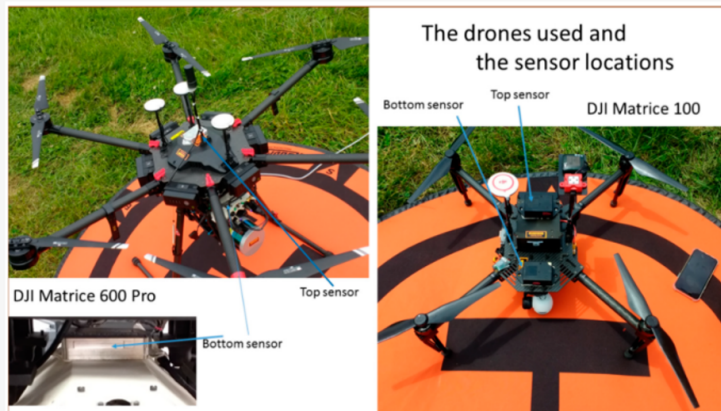


FIGURE 4.14: Drones in Experiments

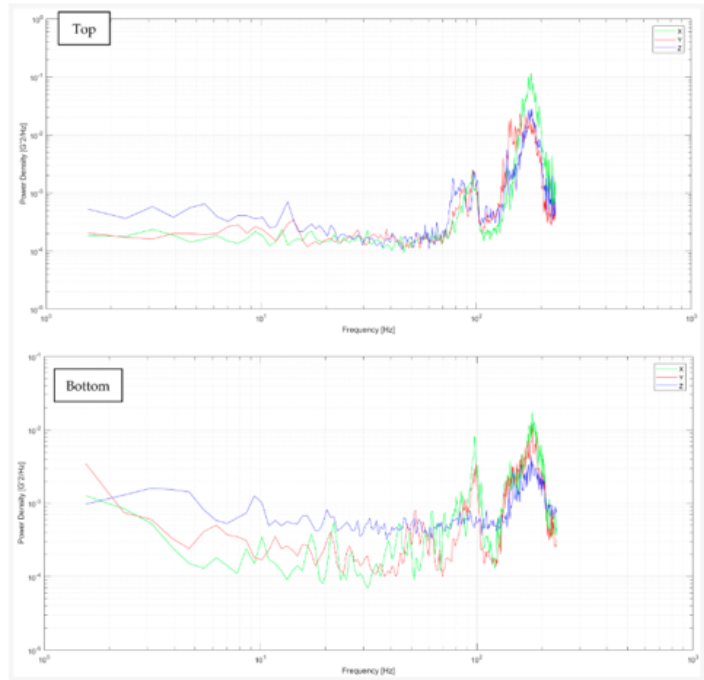


FIGURE 4.15: DJI 600

Frequency and PSD breakpoints for DJI Matrice 600 Pro top					
X-Axis (Lateral)		Y-Axis (Longitudinal)		Z-Axis (Vertical)	
Frequency (Hz)	PSD (g <sup>2</sup> /Hz)	Frequency (Hz)	PSD (g <sup>2</sup> /Hz)	Frequency (Hz)	PSD (g <sup>2</sup> /Hz)
1.56	0.000264	1.56	0.000291	1.56	0.000749
3.13	0.000335	7.81	0.000400	5.47	0.000921
77.34	0.000481	14.06	0.000483	13.28	0.001013
89.84	0.001862	28.13	0.000332	65.63	0.000442
96.09	0.003587	71.88	0.000319	78.13	0.002540
150.00	0.005751	96.88	0.003497	96.88	0.032923
164.00	0.060750	145.31	0.026648	167.97	0.021617
175.00	0.140900	160.15	0.032923	175.00	0.038123
179.68	0.165814	178.13	0.030444	210.94	0.002561
210.94	0.007295	210.94	0.011054		

Frequency and PSD breakpoints for DJI Matrice 600 Pro bottom					
X-Axis (Lateral)		Y-Axis (Longitudinal)		Z-Axis (Vertical)	
Frequency (Hz)	PSD (g <sup>2</sup> /Hz)	Frequency (Hz)	PSD (g <sup>2</sup> /Hz)	Frequency (Hz)	PSD (g <sup>2</sup> /Hz)
6.25	0.000251	6.25	0.000708	3.125	0.002264
10.16	0.000497	11.72	0.000509	9.375	0.001788
21.88	0.000773	21.09	0.000564	20.31	0.001160
80.47	0.001793	52.34	0.001130	92.96	0.001107
97.66	0.011633	99.23	0.004898	110.94	0.001150
167.19	0.007783	171.88	0.009151	173.44	0.004891
178.13	0.017958	180.47	0.017030	178.13	0.006435
181.25	0.024818	188.28	0.011457		
210.94	0.001084				

FIGURE 4.16: DJI 600

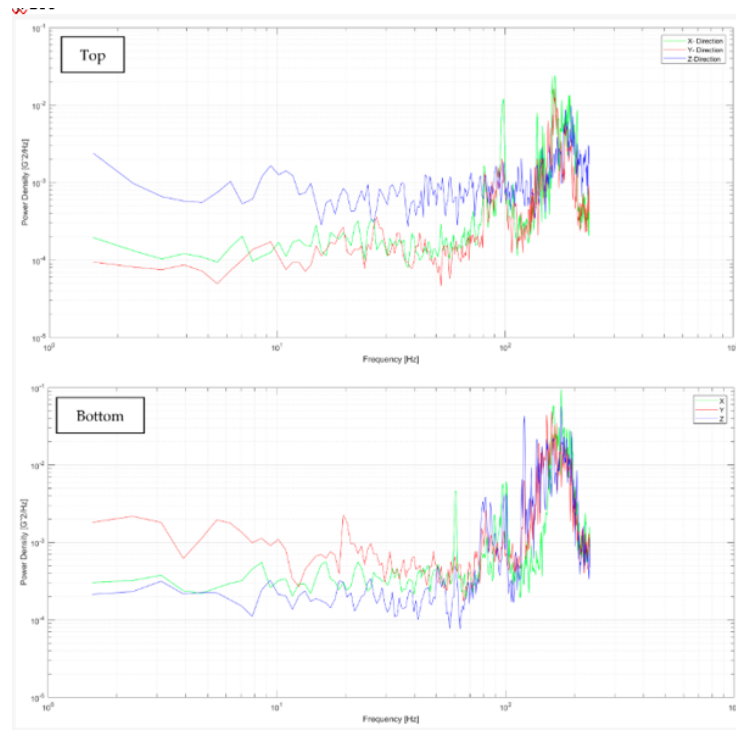


FIGURE 4.17: DJI 100

Frequency and PSD breakpoints for DJI Matrice 100 top					
X-Axis (Lateral)		Y-Axis (Longitudinal)		Z-Axis (Vertical)	
Frequency (Hz)	PSD (g <sup>2</sup> /Hz)	Frequency (Hz)	PSD (g <sup>2</sup> /Hz)	Frequency (Hz)	PSD (g <sup>2</sup> /Hz)
1.56	0.000196	1.56	0.000095	1.56	0.002401
7.03	0.000203	9.38	0.000172	6.25	0.001030
14.84	0.000282	19.53	0.000266	9.38	0.001658
19.53	0.000236	27.34	0.000360	44.53	0.001255
25.78	0.000331	81.25	0.001338	91.41	0.001867
72.66	0.000432	96.88	0.002042	117.97	0.002057
98.44	0.012128	164.06	0.016571	169.53	0.003886
165.63	0.024107			194.53	0.009995
189.84	0.013427				

Frequency and PSD breakpoints for DJI Matrice 100 bottom					
X-Axis (Lateral)		Y-Axis (Longitudinal)		Z-Axis (Vertical)	
Frequency (Hz)	PSD (g <sup>2</sup> /Hz)	Frequency (Hz)	PSD (g <sup>2</sup> /Hz)	Frequency (Hz)	PSD (g <sup>2</sup> /Hz)
3.13	0.000377	1.56	0.001820	1.56	0.000214
8.59	0.000572	5.47	0.001953	3.13	0.000316
60.15	0.004622	19.53	0.002265	9.38	0.000325
96.88	0.005804	82.03	0.002659	79.69	0.003400
161.72	0.058768	120.31	0.002689	100.78	0.004283
175.00	0.095141	139.84	0.019277	121.09	0.043357
185.15	0.029264	144.53	0.017011	136.72	0.021441
		159.38	0.049592	144.53	0.017361
		167.19	0.034629	175.00	0.056834

FIGURE 4.18: DJI 100

These graphs resembled the data from both DJI 600 and 100:

### ANSYS Model Setup

Once the PSD data was collected, we uploaded the vibration isolator model into ANSYS, a powerful finite element analysis software. The isolator geometry was defined, and the material properties of the damper and structural components were assigned based on the data provided earlier.

Damper Material: PDMS (Sylgard™ 184 Silicone Elastomer) Structural Component Material: Acrylic (PMMA) By assigning the correct material properties to each part of the model, we ensured that the simulation accurately reflected the physical properties of the vibration isolator

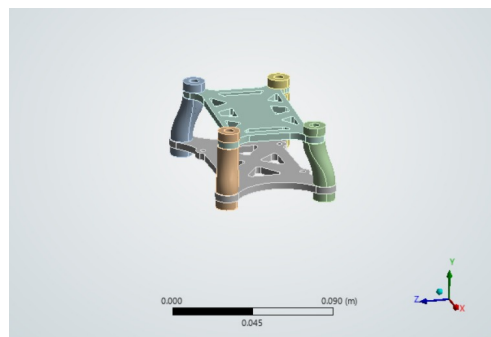


FIGURE 4.19: Damper

### Random Vibration Analysis

To simulate the random vibrations experienced by the equipment mounted on the UAV, we performed a random vibration analysis in ANSYS. This type of analysis involves applying PSD acceleration data as input to the model and calculating the system response over a range of frequencies. The results

#### 1) PSD data of dji 600 in x -axis

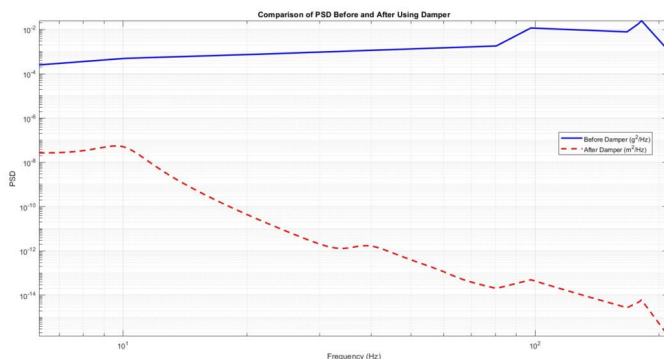


FIGURE 4.20: Comparison of PSD ( $\text{g}^2/\text{Hz}$ ) data before using damper and PSD( $\text{m}^2/\text{Hz}$ ) after using damper at random vibration test for Dji matrice 600 for x axis

## Deflection in y-axis

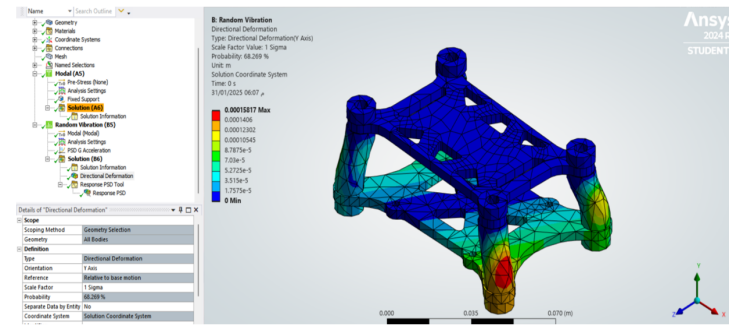


FIGURE 4.21: Deflection in Y-axis

Max deflection in y is 0.0001406 m

Rms value in y direction =  $4.3981\text{e-}013$  m

expected frequency in y direction = 14.103 Hz

## Deflection in x-axis

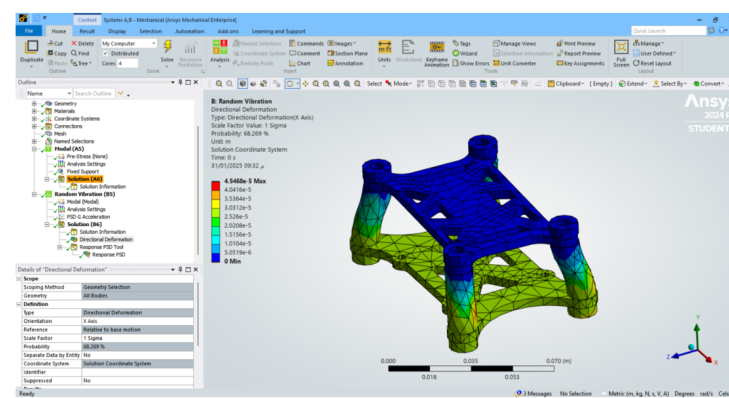


FIGURE 4.22: Deflection in X-axis

Max deflection in x axis =  $4.5468\text{e-}5$

Rms value in x direction =  $7.1308\text{e-}013$  m

expected frequency in x direction = 14.061 Hz

## Deflection in z-axis

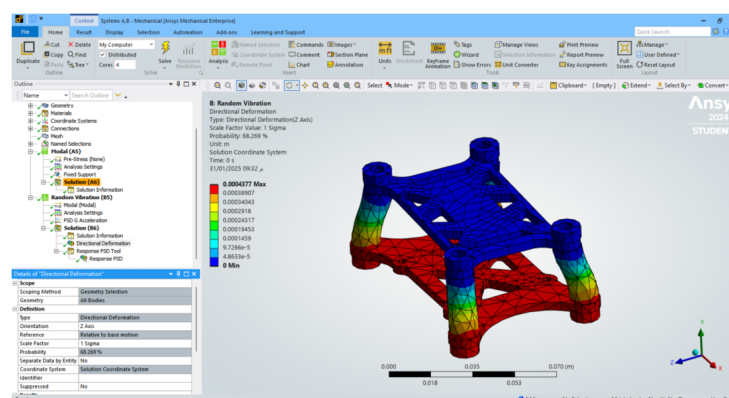


FIGURE 4.23: Deflection in Z-axis

Max deflection in z is 0.00004377  
 Rms value in z direction = 1.8403e-004 m  
 expected frequency in z direction = 11.859 Hz

## 2) PSD data of DJI 100 in x -axis

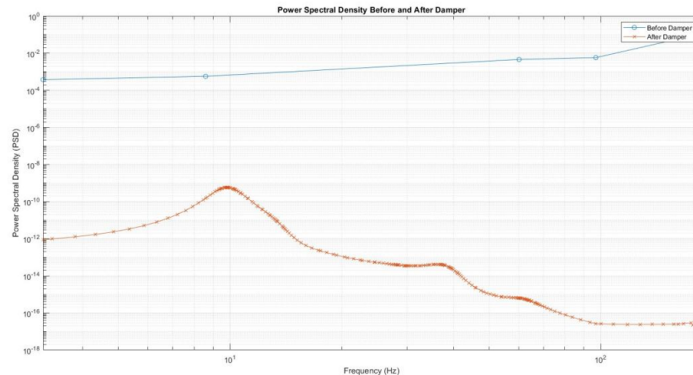


FIGURE 4.24: Comparison of PSD ( $\text{g}^2/\text{Hz}$ ) data before using damper and PSD( $\text{m}^2/\text{Hz}$ ) after using damper at random vibration test for Dji matrice 100 for x axis

## Deflection in z-axis

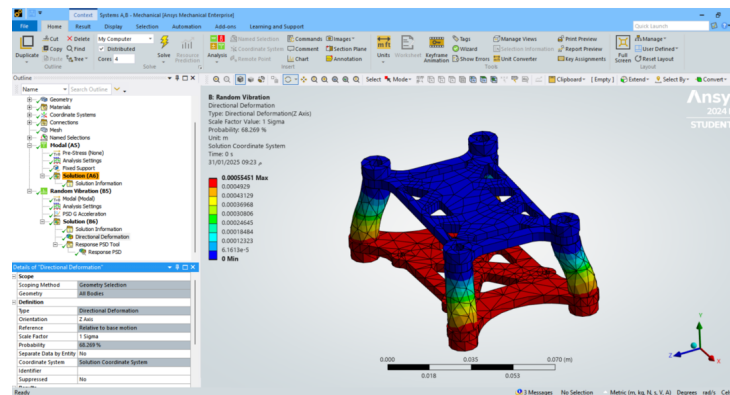


FIGURE 4.25: Z-Deflection

Max deflection in z = 0.000554851  
 Rms value in z direction = 5.5303e-004 m  
 Expected frequency in z direction = 5.6829 Hz  
**Deflection in y-axis**

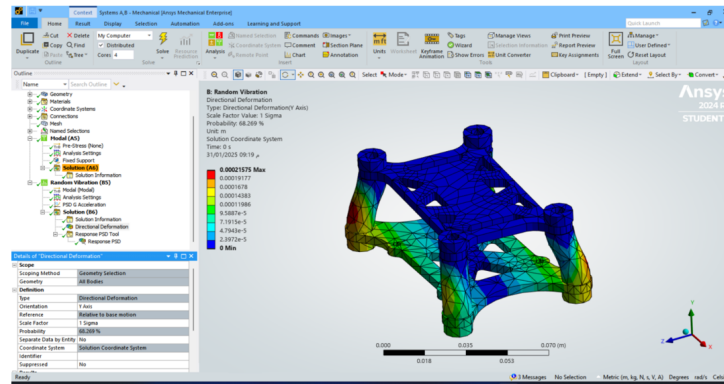


FIGURE 4.26: Y-Deflection

Max deflection in  $y=0.00021575$

Rms value in  $y$  direction =  $5.6768e-013$  m

Expected frequency in  $y$  direction =  $15.375$  Hz

### Deflection in x axis

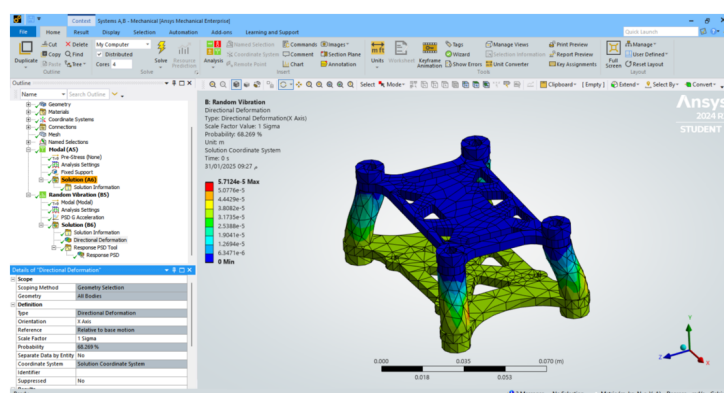


FIGURE 4.27: X-Deflection

Max deflection in  $x = 5.7124e-5$

Rms value in  $x$  direction =  $9.2026e-013$  m

Expected frequency in  $x$  direction =  $15.32$  Hz

### Results: DJI Matrice 600 Pro

- X-axis:** Max deflection =  $4.5468 \times 10^{-5}$  m, RMS =  $7.1308 \times 10^{-13}$  m, Frequency = 14.061 Hz
- Y-axis:** Max deflection =  $0.0001406$  m, RMS =  $4.3981 \times 10^{-13}$  m, Frequency = 14.103 Hz
- Z-axis:** Max deflection =  $4.377 \times 10^{-5}$  m, RMS =  $1.8403 \times 10^{-4}$  m, Frequency = 11.859 Hz

### Results: DJI Matrice 100

- X-axis:** Max deflection =  $5.7124 \times 10^{-5}$  m, RMS =  $9.2026 \times 10^{-13}$  m, Frequency = 15.32 Hz

- **Y-axis:** Max deflection =  $0.00021575$  m, RMS =  $5.6768 \times 10^{-13}$  m,  
Frequency = 15.375 Hz
- **Z-axis:** Max deflection =  $0.000554851$  m, RMS =  $5.5303 \times 10^{-4}$  m,  
Frequency = 5.6829 Hz

## Discussion

The vibration analysis was carried out on two drone platforms—DJI Matrice 600 Pro and DJI Matrice 100—to evaluate their dynamic response and the effectiveness of the damping system in mitigating structural vibrations. The assessment focused on the three principal axes (X, Y, and Z) and measured parameters such as maximum deflection, root mean square (RMS) values, and power spectral density (PSD), both before and after damping. The results confirm the attenuation of vibrational energy and the effectiveness of the damping system in enhancing stability and structural integrity.

**Results for DJI Matrice 600 Pro** The PSD data for the DJI Matrice 600 Pro revealed a significant reduction in vibrational energy after applying the damping system. The key findings are:

- **Maximum Deflections:**
  - X-axis:  $4.5468 \times 10^{-5}$  m
  - Y-axis:  $0.0001406$  m
  - Z-axis:  $4.377 \times 10^{-5}$  m
- **RMS Values:**
  - X-axis:  $7.1308 \times 10^{-13}$  m
  - Y-axis:  $4.3981 \times 10^{-13}$  m
  - Z-axis:  $1.8403 \times 10^{-4}$  m
- **Expected Frequencies:**
  - X-axis: 14.061 Hz
  - Y-axis: 14.103 Hz
  - Z-axis: 11.859 Hz

**Results for DJI Matrice 100** Similarly, the results for the DJI Matrice 100 also showed significant vibration mitigation:

- **Maximum Deflections:**

- X-axis:  $5.7124 \times 10^{-5}$  m
- Y-axis: 0.00021575 m
- Z-axis: 0.000554851 m

- **RMS Values:**

- X-axis:  $9.2026 \times 10^{-13}$  m
- Y-axis:  $5.6768 \times 10^{-13}$  m
- Z-axis:  $5.5303 \times 10^{-4}$  m

- **Expected Frequencies:**

- X-axis: 15.32 Hz
- Y-axis: 15.375 Hz
- Z-axis: 5.6829 Hz

### Key Observations

The results highlight the efficacy of the vibration isolator in reducing vibrational energy across all axes for both UAV models. Notably, the damping system demonstrated superior performance along the X and Y axes compared to the Z-axis, particularly for the DJI Matrice 100. This discrepancy is likely attributed to differences in payload distribution and structural design between the two drones.

### Conclusion

The study emphasizes the importance of selecting appropriate materials—PDMS for damping and PMMA for structural integrity—in designing vibration isolators. The findings confirm that the damping system plays a crucial role in enhancing the performance and stability of UAV platforms under dynamic loading conditions.

## 4.3 Mechanical Design Results

In mechanical design there were a list of Tests were made to ensure that the assembly would withstand and pass the criteria required so that our product could be Atex certified. The tests needed for Atex are:

1. Overpressure Test
2. Drop Test
3. Vibration analysis
4. Impact Resistance
5. Thermal tests
6. Sealing Test for Cable
7. Non-Transmission of an internal ignition

### 4.3.1 Overpressure Test

To assess the structural integrity of the Glass Reinforced Plastic (GRP) enclosure, a pressure test was conducted at 5 bar, which is more than three times the reference operating pressure of 1.5 bar. This test significantly exceeds the standard overpressure test requirement of 1.5 times the reference pressure (2.25 bar), providing a robust validation of the enclosure's resilience.

In the finite element simulation, a preload torque of 1.84 N·m was applied using M3 bolts to evaluate the mechanical response of the enclosure. The simulation results indicated that the enclosure effectively withstood three times the reference pressure, with a maximum observed stress of 239 MPa occurring at the M3 bolts. Given that the tensile strength of GRP is 250 MPa, the enclosure demonstrated sufficient mechanical robustness under extreme conditions.

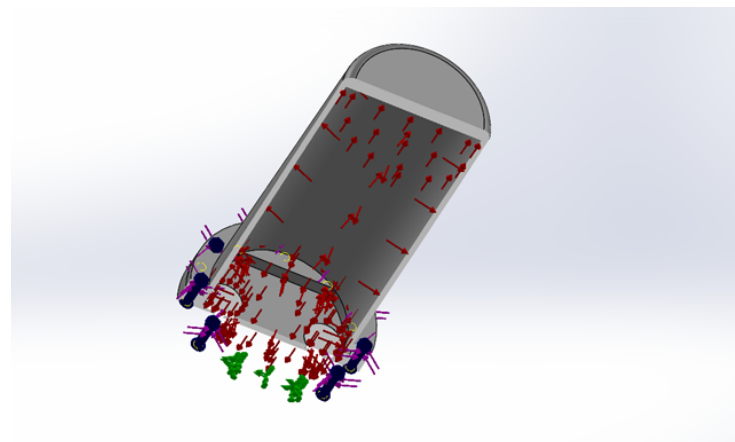


FIGURE 4.28: Forces Applied

The M3 bolts selected for the assembly are coarse-threaded, grade 12.9, with an ultimate tensile load of 6140 N and a nominal stress area of 5.03 mm<sup>2</sup>,

yielding a tensile strength of 1220 MPa. The results confirm that the bolts remain well within their structural limits under applied loading conditions.

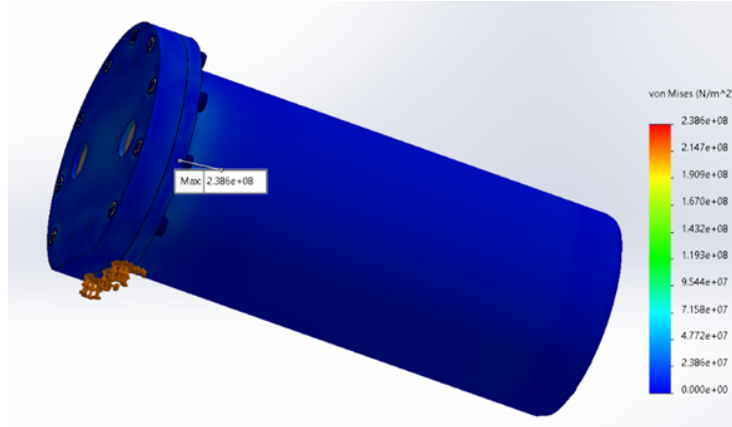


FIGURE 4.29: Stress Results in Overpressure Test

Additionally, as shown in Figure 2, the maximum displacement of the enclosure was recorded at 1 mm, occurring at three times the reference pressure. This level of deformation is within acceptable limits, ensuring the structural stability and functional reliability of the enclosure under operational and extreme pressure conditions.

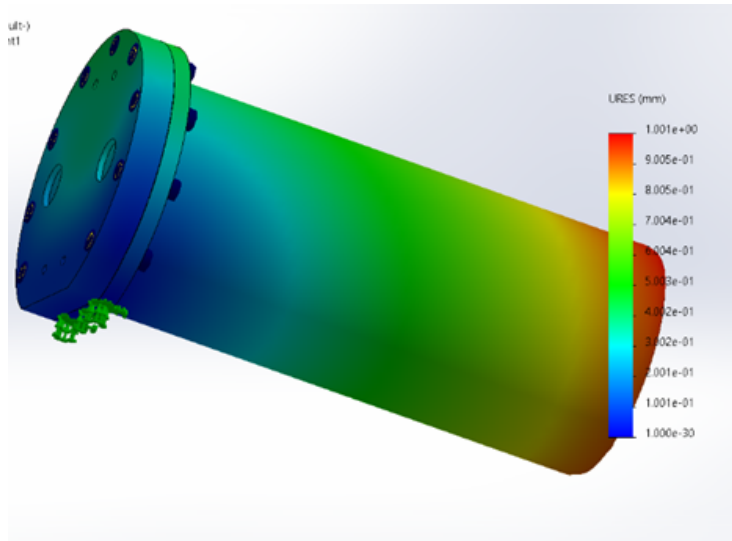


FIGURE 4.30: Displacement Results in Overpressure Test

### 4.3.2 Drop Test

In the Drop Test simulation the product is run through falls from a height of one meter, leading to acceptable stress with small acceptable instant displacement as maximum stress is smaller than 250Mpa. The Bolt connections were replaced with local bond between the surfaces of cover and gas chamber face for this test.

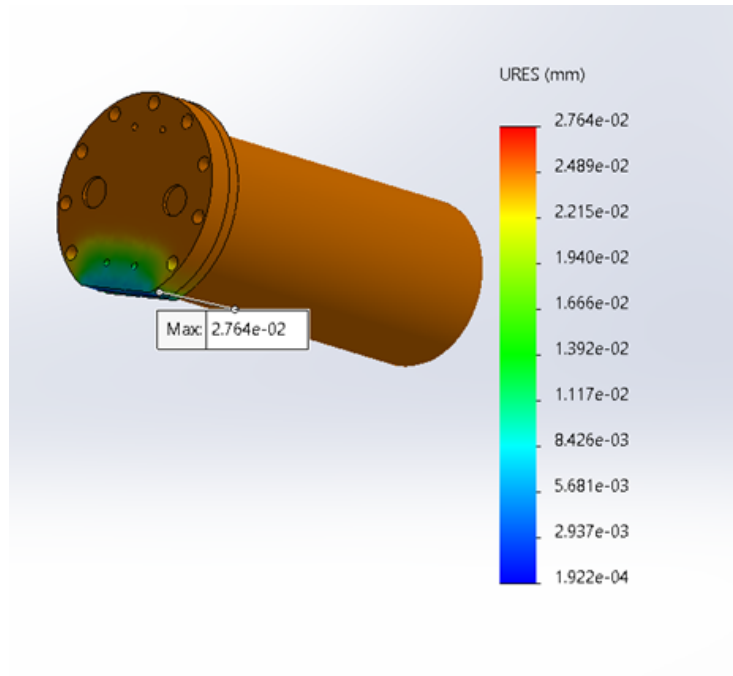


FIGURE 4.31: Displacement Results in Drop Test

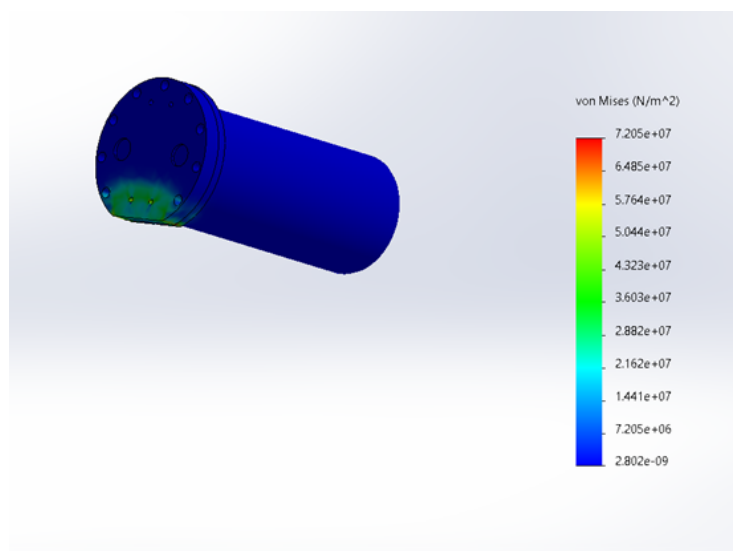


FIGURE 4.32: Stress Results in Drop Test

### 4.3.3 Vibration Analysis

In vibration analysis the first five modal shapes of each mount were obtained to ensure resonance isn't reached. The vibration analysis is used to ensure natural frequency isn't reached where the frequency range will be between 10 to 211 Hz.

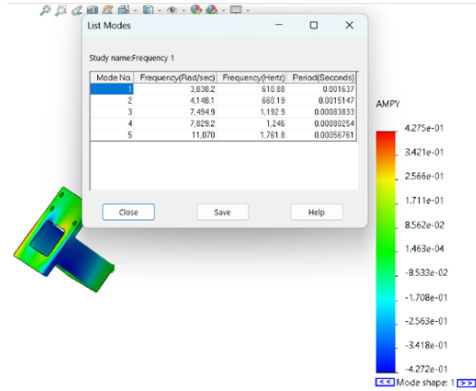


FIGURE 4.33: Natural Frequencies of Laser Mount

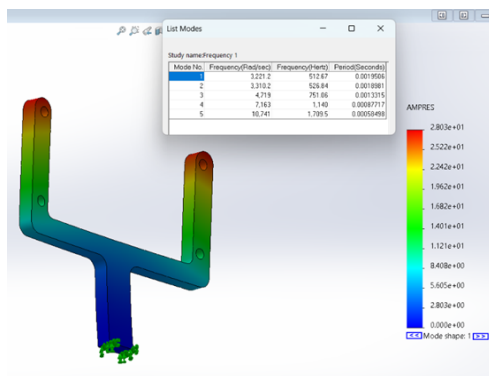


FIGURE 4.34: Natural Frequencies of PCB Mount

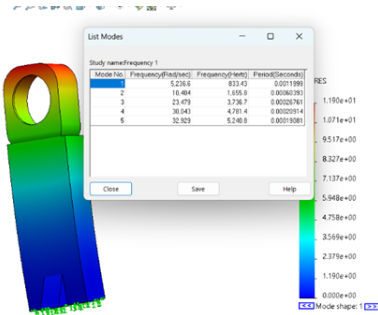


FIGURE 4.35: Natural Frequencies of Lens Mount

## Chapter 5

# Future work

### 5.1 Thermal Management Team

The next phase of this study focuses on implementing Proportional-Integral-Derivative (PID) control to optimize the thermal management system. The primary objective is to integrate a closed-loop control strategy that dynamically regulates heat dissipation, enhancing system stability and efficiency.

A micro controller-based feedback system will be introduced to control the Thermoelectric Cooler (TEC). A temperature sensor will continuously monitor the system's thermal state, providing real-time feedback to the micro controller, which will adjust the TEC's power input accordingly. This approach will ensure precise temperature regulation by mitigating fluctuations that could affect the spectroscopy sensor's performance.

The integration of PID control will further refine the thermal circuit model, enabling real-time adaptive thermal management. The physical heat dissipation system will be fine-tuned through experimental validation, ensuring that the TEC-driven cooling mechanism operates optimally under varying environmental and operational conditions.

Future work will also include extensive simulation and empirical testing to assess the system's response to transient thermal loads. These evaluations will inform design improvements, ensuring that the control system remains robust while minimizing power consumption and thermal lag.

By applying PID control to the TEC, the thermal management system will transition towards an **autonomous, self-regulating** framework, improving sensor accuracy, reliability, and operational lifespan.

### 5.2 Vibration Management Team

- Material innovation

The combination of PDMS and PMMA has shown promising results in vibration isolation and structural support. Further research should explore alternative materials that provide better damping performance, particularly addressing weaknesses in Z-axis vibration measurements. The development of advanced composite materials and hybrid polymers should focus on improving both damping

capacity and structural integrity while maintaining low thermal expansion and resistance to environmental changes.

- Optimization of material composition

Achieving higher damping efficiency and precise energy management across all axes requires refining material formulations. Special attention should be given to optimizing the PDMS mixing process to enhance vibration control.

- Integration of smart materials

The use of smart materials such as piezoelectric polymers and magnetorheological elastomers can enable real-time active vibration control. These materials adjust their properties in response to external stimuli, offering adaptive damping solutions.

- Improved geometries

The redesign of isolator shapes should be guided by material performance. Conical and hybrid-shaped isolators are potential configurations that could enhance Z-axis energy absorption and improve vibration isolation.

- Enhanced simulation models

Finite element simulation models should be expanded to analyze UAV operational conditions, environmental effects, and system movements. A more comprehensive analysis will provide deeper insights into material behavior when integrated with structural components.

- Experimental validation

Vibration isolators should be tested in various UAV systems with different payload conditions to assess their real-world performance. Experimental testing will help determine the reliability and general applicability of the proposed materials and designs.

- Sustainability considerations

The use of recyclable or eco-friendly materials in vibration isolators should be explored to align with global sustainability initiatives while maintaining high performance and durability.

### 5.3 Mechanical Design Team

Simulations have proved that our product mechanical behavior will withstand the mechanical test whether drop test or overpressure test. Simulations also showed that the parts in the assembly have natural frequency out of the range of the vibration of the environment. Consequently, resonance is avoided.

However, these simulations must be validated by experiment which must have output within 5% of the simulation output. Moreover, the necessity of replacing the breathing and draining devices with ones that are Atex certified. The final product should include explosion proof joints, placed in contact with two surfaces to ensure no escape of internal explosion into the atmosphere.

Once the test of internal explosion is conducted were specific mixture of gases are placed in the sensor beside ignition source and the enclosure should withstand the pressure and ensure no flame escaped. After validating our simulations by experiments non transmission test must be conducted to ensure no transmission of gas happens.

In the final product our pipes will be replaced with Atex metallic conduit and cemented sealing will be used at draining and breathing devices. Last but not least the product is designed to have flameproof type protection but additional protection types will require accordance with another directives for example increased safety require accordance with EN 600079-7.

## Chapter 6

# Discussion and Conclusion

### 6.1 Discussion

The study successfully demonstrated the effectiveness of the designed systems for thermal management, vibration mitigation, and mechanical stability in the gas sensor module. The key findings across these domains reinforce the validity of the proposed methodologies and highlight areas for further improvement.

#### 6.1.1 Vibration Analysis and Performance

The experimental vibration analysis conducted on the DJI Matrice 600 Pro and DJI Matrice 100 UAVs confirmed the ability of the damping system to attenuate vibrational energy along all three principal axes. The Power Spectral Density (PSD) data revealed a notable reduction in vibration amplitudes post-damping, particularly in the X and Y axes. However, a relatively higher residual vibration was observed in the Z-axis, likely due to structural and payload distribution differences across the UAV models.

The damping materials, primarily PDMS (Polydimethylsiloxane) and PMMA (Polymethyl methacrylate), exhibited favorable properties in minimizing vibration transmission. However, optimizing material composition and incorporating smart materials such as magnetorheological elastomers could further enhance real-time vibration control. Future improvements should focus on refining the isolator geometries to better absorb energy along the Z-axis while maintaining structural integrity.

#### 6.1.2 Thermal Management Effectiveness

The thermoelectric cooling (TEC) system played a crucial role in regulating the temperature of the spectroscopy sensor. The implementation of an electrical-thermal circuit analogy provided valuable insight into the system's heat dissipation behavior. The experimental validation confirmed that the designed thermal interface materials (TIM), including thermal vias, aluminum blocks, and heat pipes, contributed to maintaining stable operating temperatures.

However, the current system operates in an open-loop configuration, which introduces minor temperature deviations due to external fluctuations. The integration of a Proportional-Integral-Derivative (PID) control system in future iterations will allow for real-time feedback regulation of the TEC power input, ensuring a more stable and autonomous thermal environment.

### 6.1.3 Mechanical Integrity and Certification Readiness

Mechanical simulations and stress analyses validated the structural robustness of the gas sensor enclosure under extreme conditions. The overpressure test confirmed that the Glass Reinforced Plastic (GRP) enclosure could withstand pressures exceeding three times the reference operating limit. The finite element analysis (FEA) results showed that maximum stress concentrations occurred at the M3 bolts, which remained within their mechanical limits.

Additional validation is required through physical drop tests and impact resistance assessments to ensure compliance with industry standards such as ATEX and IP67. Replacing existing sealing and breathing components with certified explosion-proof alternatives will further improve safety and reliability.

## 6.2 Conclusion

This research successfully developed and validated a gas sensor module with integrated vibration mitigation, thermal stability, and mechanical robustness. The key contributions of this work are:

- The implementation of PDMS-based vibration isolators demonstrated significant reduction in vibrational noise, improving sensor stability.
- A thermoelectric cooling system effectively managed temperature fluctuations, with further enhancements planned through closed-loop PID control.
- Structural simulations confirmed the mechanical strength of the GRP enclosure, ensuring resilience against overpressure and environmental stressors.

The integration of multidisciplinary engineering approaches played a crucial role in optimizing sensor performance. The findings highlight that while the current design meets preliminary performance criteria, further refinement in vibration isolation, thermal feedback control, and regulatory compliance testing will enhance its readiness for deployment in industrial applications.

## 6.3 Future Directions

Future work should focus on:

- Implementing real-time PID control to optimize TEC performance and minimize thermal lag.
- Exploring advanced damping materials and improved geometric configurations to enhance Z-axis vibration isolation.
- Conducting extensive physical testing, including drop and ignition safety tests, to achieve full ATEX certification.

- Refining mechanical sealing techniques to ensure IP67 compliance and improve environmental durability.

By addressing these aspects, the system can transition from prototype validation to large-scale application in real-world industrial environments.

# Bibliography

- [1] A. Smith et al. Thermal effects in infrared gas sensors. *Journal of Sensor Technology*, 32(5):123–130, 2020.
- [2] B. Johnson and C. Lee. Optical materials for temperature-stable spectroscopy. *Applied Optics*, 45(4):456–463, 2018.
- [3] M. Gupta and T. Zhao. Thermoelectric cooling in ir spectroscopy sensors. *Sensors and Actuators A: Physical*, 300:1–8, 2021.
- [4] J. Lin et al. Passive thermal management strategies for mems devices. *Microelectronics Journal*, 98:45–56, 2019.
- [5] R. Kim et al. Thermal properties of mems materials for gas sensing applications. *Sensors*, 19(10):1234–1245, 2020.
- [6] D. Wang et al. Real-time thermal compensation in infrared spectroscopy. *IEEE Sensors Journal*, 21(12):13456–13464, 2022.
- [7] S. Nguyen and A. Patel. Vibration-induced noise in gas sensors. *IEEE Transactions on Instrumentation and Measurement*, 69(11):5678–5685, 2020.
- [8] P. Kumar et al. Damping materials for portable gas sensors. *Journal of Materials Science*, 55(4):1234–1248, 2019.
- [9] T. Akbar and L. Wei. Vibration isolation in mobile spectroscopy systems. *Review of Scientific Instruments*, 92(7):1–10, 2021.
- [10] F. Li et al. Piezoelectric vibration control in mems sensors. *Microsystem Technologies*, 27(2):679–688, 2020.
- [11] K. Park et al. Dual-beam compensation in ir spectroscopy. *Sensors and Actuators B: Chemical*, 320:1–9, 2021.
- [12] AIP Publishing. Design and application of a high-pressure combustion chamber for ... *Journal of Applied Physics*, 2019.
- [13] Fluid Sealing Association. *Gasket Handbook - 1st Edition*. Fluid Sealing Association, 2017.
- [14] Katie Schwertz. *Optomechanical Design and Analysis*. SPIE Press, 2020.
- [15] John H. Lau et al. *MEMS Packaging*. Springer, 2018.
- [16] Mahmoud M. Reda Taha et al. Chemical resistance and mechanical properties of glass fiber-reinforced plastic pipes for oil, gas, and power-plant applications. *Materials and Design*, 67:207–219, 2015.

- [17] European Commission. *ATEX Guidelines - 4th Edition*. European Commission, 2016.
- [18] ATEQ USA. Ip67 waterproof leak testing: What you need to know. *ATEQ Technical Bulletin*, 2024.
- [19] Y. Zhang et al. Integrated thermal and vibration management in mems gas sensors. *Sensors*, 22(6):1234–1245, 2022.
- [20] H. Liu et al. Multiphysics simulation for gas sensor design. *Journal of Computational Physics*, 400:1–15, 2021.
- [21] Simon Lineykin and Sam Ben-Yakov. Analysis of thermoelectric coolers by a spice-compatible equivalent-circuit model. *IEEE Power Electronics Letters*, 3(2):63–66, June 2005.
- [22] ProtoExpress. Thermal via calculator, 2025.
- [23] António B. Pereira, João M. S. Dias, José P. Rios, Nélia M. Silva, Sathishkumar Duraisamy, and Ana Horovistiz. Brazing of copper pipes for heat pump and refrigeration applications. *Metals*, 14(2):171, 2024.
- [24] Wakefield Thermal. *Heat Pipe Selection Guideline*, r3 edition, 2020. Accessed: 2025-02-01.
- [25] C. Ge, K. Dunno, M. A. Singh, L. Yuan, and L.-X. Lu. Development of a drone's vibration, shock, and atmospheric profiles. *Applied Sciences*, 11(11):5176, 2021.
- [26] Y. Legovich, Y. Maximov, and D. Maximov. Quadrocopter vibration damping. In *13th International Large-Scale Conference "Management System of Development" (MLSD)*, 2020.
- [27] Y.-H. Shin, D. Kim, S. Son, J.-W. Ham, and K.-Y. Oh. Vibration isolation of a surveillance system equipped in a drone with mode decoupling. *Applied Sciences*, 11(4):1961, 2021.
- [28] F. Ahmed, J. Mohanta, A. Keshari, and P. S. Yadav. Recent advances in unmanned aerial vehicles: a review. *Arabian Journal for Science and Engineering*, 47(7):7963–7984, 2022.
- [29] Y. Cai, E. Lam, T. Howlett, and A. Cai. Spatiotemporal analysis of “jello effect” in drone videos. In *Advances in Human Factors in Robots and Unmanned Systems: Proceedings of the AHFE 2019 International Conference on Human Factors in Robots and Unmanned Systems*, page 10, Washington DC, USA, 2020.
- [30] R. M. Morales, M. C. Turner, P. Court, R. Hilditch, and I. Postlethwaite. Force control of semi-active valve lag dampers for vibration reduction in helicopters. *IET Control Theory Applications*, 8(6):409–419, 2014.
- [31] S. Radkowski and P. Szulim. Analysis of vibration of rotors in unmanned aircraft. In *2014 19th International Conference on Methods and Models in Automation and Robotics (MMAR)*, 2014.

- [32] S. Sundararaj, K. Dharsan, J. Ganeshraman, and D. Rajarajeswari. Structural and modal analysis of hybrid low altitude self-sustainable surveillance drone technology frame. *Materials Today: Proceedings*, 37:409–418, 2021.
- [33] A. Oakey, T. Waters, W. Zhu, P. G. Royall, T. Cherrett, P. Courtney, and N. Jelev. Quantifying the effects of vibration on medicines in transit caused by fixed-wing and multi-copter drones. *Drones*, 5(1):22, 2021.
- [34] G. Redde, P. Kulkarni, P. Patil, D. Khedkar, and J. Chopade. Vibration analysis on frame and propeller of drone. *International Journal of Advance Research in Science and Engineering*, 7(5):1–10, 2018.
- [35] Dow Inc. Sylgard™ 184 silicone elastomer kit, n.d. Accessed: 2025-02-01.
- [36] J. Smith. Solar panel efficiency: The impact of tilt and orientation. *Renewable Energy Journal*, 15(4):203–215, 2020.
- [37] D. Miller. Heat transfer in vertical and inclined surfaces. *Journal of Thermal Engineering*, 17(2):45–63, 2021.
- [38] L. Johnson and R. Patel. Fluid dynamics and structural impacts of vertical and inclined surfaces. *Engineering Science Review*, 12(3):98–112, 2019.
- [39] B. Anderson. Aerodynamics of tilted and vertical plates: A comparative study. *Aerospace Research*, 10(1):23–40, 2018.
- [40] T. Wilson and M. Carter. Structural load distribution in cylindrical and conical forms. *Structural Engineering Journal*, 20(5):187–202, 2022.
- [41] P. Robinson. Manufacturing considerations for s-shape, cylindrical, and conical components. *Industrial Manufacturing Journal*, 14(7):311–329, 2020.
- [42] Laird Thermal Systems. *PowerCycling PCX Series PCX4-7-F1-2020-TA-RT-W6 Datasheet*. Laird Thermal Systems, Inc., June 2022. Revision: 00, Date: 06-01-2022, Print Date: 06-10-2022.
- [43] K.-J. Bathe. *Finite Element Procedures*. Prentice Hall, 2014.
- [44] Dow Inc. Fascinating silicones, n.d. Accessed: 2025-02-01.
- [45] X. Huang and R. K. Prud'homme. Applications of thiol–ene click chemistry to polymeric materials from new thermoset plastics to polymer bioconjugates. *Chemistry of Materials*, 18(24):5727–5735, 2006.